High Harmonic Generation using a 2 μm OPCPA

Clemens Tobias Friedrich Jakubeit

München 2019

High Harmonic Generation using a 2 μm OPCPA

Clemens Tobias Friedrich Jakubeit

Dissertation
an der Fakultät für Physik
der Ludwig–Maximilians–Universität
München

vorgelegt von
Clemens Tobias Friedrich Jakubeit
aus Starnberg

München, den 15.04.2019

Erstgutachter: Ferenc Krausz
Zweitgutachter: Eleftherios Goulielmakis
Tag der mündlichen Prüfung: 15.05.2019

Für Tizian

Contents

List of Figures

Preface

The human pursuit for a better understanding of the world surrounding us can be separated into two very rough and simultaneously very big questions. "What is?" and "What is happening?". What is everything made of and what is it doing, how is it behaving? Attempts to answer the former question led to models like the surprisingly accurate "Atomism" by Leucippus and Democritus [1] around the fifth century BCE in ancient Greece or the much less accurate idea that everything could consist of the five elements fire, water, earth, air, and aether [2] also from ancient Greece. Our current, by far not complete, understanding includes the standard model of elementary particles for "normal" matter, the not really complete idea of dark matter and the even more abstract idea of dark energy. Famous theories like classical mechanics or electro dynamics, as well as our current approaches of quantum mechanics or the theory of relativity mostly try to answer the latter question: "What is happening?". The closer we look, however, it gets clear that these questions are not really separable. The standard model links forces to particles, quantum mechanics successfully predicted previously unknown particles. Despite this mixing at the most fundamental level, the topic of this thesis can be related to the latter question. The goal is to experimentally investigate what is happening and to do so on a timescale close to the limit of what we currently can achieve.

The basis for our progress in the understanding of our world is its observation. Although it is the resulting theories that really let us understand, first we need to see what is happening. We came a long way in our means to do so. From Newton's apple (although regrettably most likely a made up story) we went to build devices like ATLAS at CERN to look into the very core of matter and its mechanisms [3] or LIGO to investigate fundamental properties of space [4]. Our ability to look at dynamics in detail and with that a key to "What is happening?" evolved on a similar scale. A first step to overcome the limitations of what the human body can directly temporally resolve was the famous series of photos taken by Eadweard Muybridge. It answered the question if a horse has all its legs in the air at once during gallop [5]. Triggering a series of cameras via threads pulled by the horse itself while passing, he could brake down the previously unclear motion into a series of clear pictures, one showing all legs in the air. The subject of this thesis is providing the means to do just that, in the extreme. We are not looking at horses or other everyday items anymore. We follow the evolution of electronic excitations, resolve the waveform of light pulses, and investigate the behavior of atoms, molecules, and solids. The progress in laser technology lets us trigger, control, and measure what electrons are doing on their

own timescale. The attosecond pulses generated with high harmonic generation are the fastest humanly controllable events. But in the end the question is always "What is it really doing? Does it have its legs in the air?"

Zusammenfassung

Die umfassende Untersuchung der Dynamik eines physikalischen Prozesses erfordert die Fähigkeit, ihren Verlauf mit ausreichender zeitlicher Auflösung aufzunehmen. Bei konventionellen Kameras wird der Einfluss der Verschlusszeit offensichtlich, wenn man versucht dynamische Prozesse detailliert aufzunehmen. Die schnellsten momentan zur Verfügung stehenden Zeitlupenkameras kommen mit Belichtungszeiten im Bereich von Mikrosekunden aus und erreichen Bildraten von bis zu einer Million Bildern pro Sekunde. So beeindruckend diese Werte sind, so ist dies doch immer noch um neun Größenordnungen zu langsam für die Zeitskala elektronischer Prozesse in Atomen, Molekülen und Festkörpern, der Femtosekunden-Attosekundenzeitskala. Ultrakurze Laserpulse und die mit ihnen via Hoher-Harmonischer-Erzeugung erzeugten Attosekundenpulse können diese gewaltige Lücke überwinden und erlauben Einblicke in die elektronischen Zustände von Materie. Die hier präsentierten Arbeiten untersuchen einen möglichen Weg diese Fähigkeit noch auszuweiten. Hohe-Harmonischen-Erzeugung und damit die Erzeugung von Attosekundenpulsen ist mittlerweile ein wohletabliertes Verfahren. Unter Verwendung von Titan:Saphir Lasern mit einer Wellenlänge von $\lambda = 800\ nm$ können Pulse mit einer Dauer von unter 100 as routinemäßig erzeugt werden, wobei die Energien der generierten Photonen über einen weiten Bereich, von ein paar wenigen bis deutlich über einhundert Elektronenvolt, den experimentellen Anforderungen angepasst werden können. Dennoch gibt es Beschränkungen, die nicht ohne gravierende Änderungen des experimentellen Aufbaus zu überwinden sind. Insbesondere eine Änderung der Wellenlänge des verwendeten Lasers kann sich dabei vorteilhaft in mehreren Punkten auswirken.
Um Attosekundenpulse experimentell zu nutzen, werden diese häufig im Zusammenspiel mit ihrem erzeugenden Laser in Anreg-Abfrage-Versuchen verwendet. Die Fähigkeit die Wellenlänge und damit die Photonenenergie des verwendeten Lasers zu ändern ermöglicht die Untersuchung ganz neuer Klassen von Stoffen. Mit größerer Wellenlänge werden Effekte, die von dem Sub-Zyklus-Verlauf des elektrischen Feldes abhängen, einfacher zu messen, da hierdurch die zeitliche Auflösung relativ zu einem Zyklus zunimmt. Der der Hohen-Harmonischen-Erzeugung zugrunde liegende Mechanismus hat inhärente Beschränkungen für die erreichbaren Photonenenergien. Obwohl es keine theoretische Grenze für die atomare Reaktion gibt, so ergibt sich doch aus den Bedingungen für die Phasenanpassung, dass eine Erhöhung der Pulsenergie eines üblichen 800 nm Lasers nicht zu einer Erhöhung der Photonenenergie deutlich über 160 eV führt. Angesichts der Abhängigkeit $E_{cut} \propto \lambda^2$ [6] der spektralen, hochenergetischen Beschränkung hoher Harmonischer (high

energy cut-off), ist offensichtlich, dass eine Vergrößerung der Wellenlänge auch in diesem Punkt von Vorteil sein kann. Wie leider häufig ist auch hier eine Änderung, vorteilhaft in einer Beziehung, nachteilig in einer anderen. Die Abnahme der Konversionseffizienz mit einem Faktor von λ^{-6} (section 1.4.2), macht den Wechsel der Wellenlänge nicht so trivial, wie er zunächst erscheinen mag.
In letzter Zeit wurde von immer mehr erfolgreichen Versuchen berichtet, die Wellenlänge des antreibenden Lasers in den nahen Infrarotbereich zu verschieben, wobei sogar neue Rekorde für die Dauer der erzeugten Attosekundenpulse aufgestellt werden konnten [7, 8]. In dieser Dissertation beschreibe ich sowohl unseren erfolgreichen Versuch dies zu tun, als auch die nichttrivialen experimentellen Anforderungen, die diesen Wechsel, insbesondere für ultrakurze Pulse mit wenigen Zyklen, zu einer Herausforderung machen. Vielen Gruppen, die an dieser Aufgabe arbeiten, ist gemein, dass sie optisch parametrische Verstärker als antreibenden Laser verwenden. Was unser System, meines Wissens nach, einzigartig macht, ist seine Verstärkungsbandbreite, die Pulse mit einer Dauer von unter zwei Zyklen direkt unterstützt und dadurch die erreichbaren Pulsenergien erhöht. Im Gegensatz zu dem üblichen Ansatz eines schmalbandigen Verstärkers, gefolgt von spektraler Verbreiterung und Rekompression, verstärken wir die volle Bandbreite in einer dreistufigen OPA. Wie sich herausstellte, führt dieser Ansatz zu Herausforderungen, die in dem üblichen Schema unbekannt oder zumindest deutlich reduziert sind. Der an sich wohlbekannte Effekt der Sättigung verursacht räumlich-zeitliche Störungen des Strahls sowie des Pulses, die effiziente Hohe-Harmonischen-Erzeugung verhindert. Ich präsentiere hier unsere Beobachtungen und unsere Lösungen zur Überwindung dieser Hindernisse.
Nachdem die Hohe-Harmonischen-Erzeugung erfolgreich implementiert werden konnte, war es mir möglich die erzeugten Pulse experimentell zu nutzen. Die Technik des Attosekundenstreakings konnte etabliert werden und damit das elektrische Feld unseres Lasers vermessen werden. Frühere Ergebnisse für die Pulsdauer aus Messungen mit "Electro optic sampling" (EOS) und "Frequency resolved optical gating" (FROG) konnte ich bestätigen.
Im Zuge einer Machbarkeitsdemonstration konnte ich zeigen, dass wir in der Lage sind verschiedene Photoemissionsprozesse von Neon, mit unterschiedlichen verbleibenden ionischen Zuständen, in einem Attosekundenstreaking aufzulösen und ihre relative Emissionsverzögerung zu messen. Dies zeigt die Eignung des Systems für zukünftige Experimente.
Mit den Ergebnissen dieser Arbeit wurde die OPCPA, die für diese Dissertation verwendet wurde, bereits jetzt so modifiziert, dass das räumlich-zeitliche Profil der erzeugten Infrarotpulse verbessert werden konnte. Hiermit sollte es möglich sein, die Konversionseffizienz der Hohen-Harmonischen-Erzeugung deutlich zu steigern. Obwohl HHG vermutlich der dafür empfindlichste Prozess ist, so ist doch zu erwarten, dass dies die Eignung der OPA auch für andere feldauflösende Attosekundenexperimente verbessert hat. Die Resultate dieser Dissertation können dazu beitragen unser Verständnis und unsere Möglichkeiten zur Untersuchung der Welt auf ultrakurzen Zeitskalen zu verbessern.

Abstract

A conclusive investigation of the dynamics of a physical process requires the ability to record its evolution with sufficient temporal resolution. Using conventional cameras, the dependence on the shutter speed becomes apparent when attempting to record dynamic events in detail. The fastest available slow motion cameras achieve exposure times of only microseconds with frame rates up to one million frames per second. As impressive as these techniques are, they are still nine orders of magnitude too slow for the timescale of electronic processes in atoms, molecules, and solids, the femtosecond-attosecond timescale. Ultra short laser pulses and especially the attosecond pulses generated with them via high harmonic generation are able to bridge that huge gap and to allow insight into the evolution of electronic states in matter. The work presented in this thesis represents an investigation into one route to improve this ability even further.

High harmonic generation and with it the generation of attosecond pulses is by now a well established technique. Using Titanium Sapphire based laser systems with a central wavelength around $\lambda = 800\ nm$, pulses with durations below 100 as can be produced routinely. The generated photon energies can be adapted to the experimental requirements over a large range, from a few electron volts up to well above one hundred electron volts. Still, there are limitations that can not be overcome without significant changes in the established setup. Especially a change in the driving laser's wavelength can be beneficial in many regards.

To utilize attosecond pulses, they are often used conjointly with their generating laser in pump-probe setups. Being able to use different wavelengths, and therefore photon energies, for the driver opens the door to new classes of materials to investigate. With an increased wavelength, effects depending on the temporal sub-cycle evolution of the field get easier to resolve. A longer wavelength increases the resolution relative to the period of a cycle. The mechanism behind HHG places intrinsic limitations on the obtainable photon energies. Although there is no theoretical limit to the atomic response, because of the phase matching requirements of the process, higher pulse energies of the 800 nm driving laser can not increase the photon energies significantly beyond 160 eV. Looking at the equation for the high energy cut off of the high harmonic spectrum with $E_{cut} \propto \lambda^2$ [6], it is obvious that a change in wavelength can also be beneficial in this regard. As usual, however, a change advantageous in one regard is often detrimental in others. The conversion efficiency regrettably decreases with a factor of up to λ^{-6} (section 1.4.2), making the change not as straight forward as it might seem at first.

Recently more and more successful attempts to shift the driving wavelength into the near infrared have been reported, even setting new records in XUV pulse duration [7, 8]. In this thesis I am describing our successful attempt to do so and the non-trivial experimental factors which cause this wavelength scaling to not be straight forward in the few cycle regime. Many groups working on this challenge have in common that they are using optical parametric amplification to generate the driving pulse. What makes our system, to my knowledge, unique is that we are using a broadband amplification scheme supporting < 2 cycle pulses, increasing the possible pulse energies. While the common approach is to first use a narrow band amplifier, then spectrally broaden, and recompress afterwards, we are amplifying the full bandwidth in a three stage OPA. This amplification scheme proved to result in challenges unknown or significantly reduced in the former. The effect of saturation, that is in principle well known, causes spatio-temporal distortions in the beam and pulse that prevent efficient high harmonic generation. Presented here are observations of, and methods to overcome said obstacles.

After high harmonic generation itself could be implemented successfully, I managed to proceed to utilize the generated pulses. I could establish attosecond streaking and with it measure the electric field of our driving laser, confirming the pulse duration previously measured with frequency resolved optical gating (FROG) and electro optic sampling (EOS). These results as well as the setup is presented.

As a proof of concept experiment I could show that we are able to resolve photoemission processes in neon leaving the ion in different energy configurations via attosecond streaking and measure the emission delay between them, demonstrating the system's potential for further experiments.

With the discoveries made during this thesis' work in mind the OPCPA used for this work has already been modified to improve the spatio-temporal profile of the generated infrared pulses. With this it should be possible to increase the conversion efficiency of high harmonic generation significantly. While HHG is probably the most sensitive to these improvements, it is to be expected that the overall suitability of the OPA for a variety of experiments in electric-field-resolved attosecond science experiments will be improved. The findings from this thesis can contribute to improve our understanding of and ability to investigate the world on the ultra-fast timescale.

Chapter 1

Theoretical Overview

The ab initio theory describing the processes relevant for this thesis is extensive and far beyond what is possible to describe here. I will only try to give a brief overview of the fundamentals of the laser pulses used and the processes required for the experimental work here and refer to the relevant literature for a more in depth understanding. For a very broad basic overview of all optical topics I would refer to "Fundamentals of Photonics" by Saleh, Teich [9].

1.1 Ultrashort Pulses

1.1.1 A bit of History

The basis for all experiments described in this thesis is our ability to generate pulses with durations in the regime of atomic and molecular processes, in the femtosecond and attosecond regimes. These pulse durations of only a few cycles of the electric field make it possible to look at effects depending directly on the electric field, not only intensities. At the same time the confinement of the optical energy to these short periods provides electrical field strengths and intensities previously impossible to generate. The realization of the benefits of short optical pulses and the race for ever shorter ones started not long after the first laser was built by Maiman in 1960 [10]. Only two years later the technique of Q-switching [11] was demonstrated, followed by mode-locking [12] after two more years generating pulses in the regime of nanoseconds. The picosecond and longer femtosecond regime could already be reached with dye lasers in 1981 [13]. The discovery of Kerr lens mode locking in 1991, and especially its application to Titanium:Sapphire systems [14], finally opened the door to the world of single digit femtosecond pulses, the regime we by now work in routinely. But the development did not stop at shorter laser pulses. The observation of high harmonic generation in gases by McPherson et al in 1987[15] and finally the isolation of a single attosecond pulse by Drescher et al in 2001[16] using these ultra short laser pulses made the regime of sub femtosecond science and therefore the observation of atomic and molecular electronic processes accessible directly in the time domain.

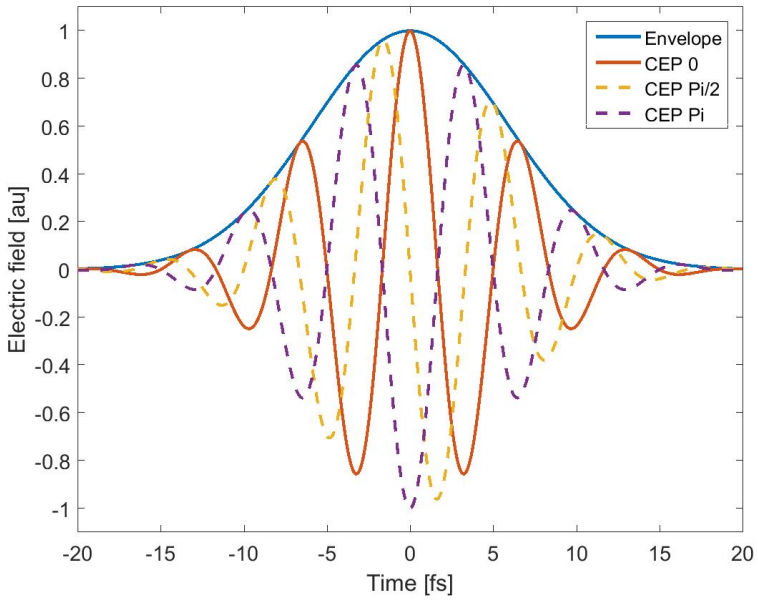

Figure 1.1: Electric field and envelope in the time domain. The graph with the solid line shows a CEP of 0, the dashed ones CEPs of $\frac{\pi}{2}$ and π respectively.

1.1.2 Theoretical Description of Pulses

I will limit my description of optical pulses to the electric field. While the magnetic component of course is not irrelevant it is neglected in the description of the effects discussed in this thesis.
In the time domain the electric field as it is plotted in section 1.1.2 can be described by:

$$\begin{aligned} E(t) &= A(t) \cdot e^{i\varphi(t)} + c.c. \\ \varphi(t) &= \omega_0 t + \phi(t) + CEP \end{aligned} \tag{1.1}$$

with $E(t)$ the electric field, $A(t)$ the envelope of the electric field, and $\varphi(t)$ the temporal phase. Often it is helpful to separate the temporal phase $\varphi(t)$ into the component describing the oscillations with the central frequency ω_0 and additional phase components $\phi(t)$ as well as the carrier envelope phase offset (CEP). While the CEP can be neglectable in many applications, especially with longer pulses, it can be a deciding factor at pulse durations of only a few cycles as it significantly changes the peak field strength and general behavior of the field. Section 1.1.2 is showing the idealized case of $\phi(t) = 0$ with different CEP values. In the temporal representation many intuitive quantities like central frequency, carrier envelope phase, or pulse duration can be understood easily. A linear chirp can for example be written as a time dependent variation in the frequency.

$$\begin{aligned} \phi(t) &= \omega_c \cdot t^2 \\ \varphi(t) &= (\omega_0 + \omega_c \cdot t)t \end{aligned} \tag{1.2}$$

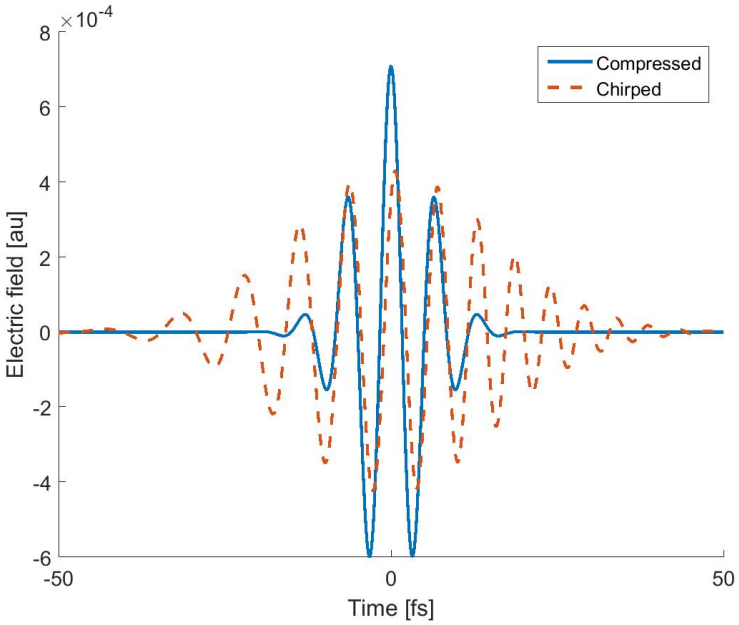

Figure 1.2: Electric field of a compressed $\psi(\omega) = 0$ and a stretched $GDD = 80\ fs^2$ pulse.

For the important understanding of pulse stretching and compression by dispersive materials however the description in the spectral domain is much more useful since in this representation it can be described through a simple multiplicative phase factor rather than a convolution. Since both representations are connected via a Fourier transform $E(\omega) = \mathcal{F}\{E(t)\}$ they are of course equivalent. Again we can separate Amplitude and phase:

$$E(\omega) = A(\omega) \cdot e^{-i\psi(\omega)} \tag{1.3}$$

where $A(\omega)$ is the spectral amplitude with its square $A(\omega)^2$ the spectral intensity, the magnitude a usual spectrometer measures. For the treatment of dispersive effects and the classification of phase behavior it is convenient to expand the spectral phase in a Taylor series

$$\begin{aligned}\psi(\omega) =& CEP + GD \cdot (\omega - \omega_0) + \frac{GDD}{2} \cdot (\omega - \omega_0)^2 + \\ &+ \frac{TOD}{6} \cdot (\omega - \omega_0)^3 + \frac{FOD}{24} \cdot (\omega - \omega_0)^4 + \dots\end{aligned} \tag{1.4}$$

with the group delay GD, the group delay dispersion GDD, third and fourth order dispersion TOD and FOD. Of course this series can be extended to any number of terms. The advantage of this description is that the effect of most optical materials on these orders is well known and can easily be calculated. The afore mentioned linear chirp in this representation means a non-zero GDD term. For the treatment of compression (or stretching) of pulses this representation is most useful. While CEP and GD can be neglected for this an ideally compressed pulse means that all other orders are equal to

zero. Section 1.1.2 shows a compressed pulse as well as one where $GDD = 80\ fs^2$. The increase in frequency with time in the second case is well visible and is what equation (1.2) describes showing again the equivalence of the spectral and temporal description.

1.2 Nonlinear Optics and Maxwells Equations

Everything described previously in section 1.1 is from the regime of linear optics meaning that the material response and its effects on the light is independent of the light's intensity. For low intensity fields this is a good approximation and the description of classical optics is correct. The processes most relevant to this thesis however are beyond the limits of it. The intensities we reach with lasers and especially ultrashort pulses need an extension of the theory including effects influenced by the intensity of the involved fields.
We start with Maxwell's equations:

$$\begin{aligned} \vec{\nabla} \cdot \vec{D} &= \rho \\ \vec{\nabla} \cdot \vec{B} &= 0 \\ \vec{\nabla} \times \vec{E} &= -\frac{\partial}{\partial t}\vec{B} \\ \vec{\nabla} \times \vec{H} &= \vec{j} + \frac{\partial}{\partial t}\vec{D} \end{aligned} \tag{1.5}$$

For non-magnetic, neutral media we can assume

$$\begin{aligned} \rho &= 0 \\ \vec{j} &= 0 \\ \vec{B} &= \mu_0 \vec{H} \\ \vec{D} &= \epsilon_0 \vec{E} + \vec{P} \end{aligned} \tag{1.6}$$

With that the curl equations become

$$\begin{aligned} \vec{\nabla} \times \vec{E} &= -\frac{\partial}{\partial t}\vec{B} \\ \vec{\nabla} \times \vec{B} &= \mu_0 \frac{\partial}{\partial t}\vec{D} \end{aligned} \tag{1.7}$$

By taking the curl of the first equation, switching the order of the derivatives and inserting the second we get

$$\begin{aligned} \vec{\nabla} \times \vec{\nabla} \times \vec{E} &= -\mu_0 \frac{\partial^2}{\partial t^2}\vec{D} \\ &= -\frac{1}{c^2}\frac{\partial^2}{\partial t^2}\vec{E} - \mu_0 \frac{\partial^2}{\partial t^2}\vec{P} \\ &= -\frac{1}{c^2}\frac{\partial^2}{\partial t^2}\vec{E} - \mu_0 \frac{\partial^2}{\partial t^2}(\vec{P}_1 + \vec{P}_{NL}) \end{aligned} \tag{1.8}$$

With the identities

$$\begin{aligned} \vec{\nabla} \times \vec{\nabla} \times \vec{E} &= \vec{\nabla} \cdot (\vec{\nabla} \cdot \vec{E}) - \vec{\nabla}^2 E \\ \vec{P}_1 &= \epsilon_0 \chi^{(1)} \vec{E} \\ n^2 &= 1 + \chi^{(1)} \end{aligned} \tag{1.9}$$

this gives the nonlinear wave equation in the usual form

$$-\vec{\nabla}^2 \vec{E} + \frac{n^2}{c^2} \frac{\partial^2}{\partial t^2} \vec{E} = -\mu_0 \frac{\partial^2}{\partial t^2} \vec{P}_{NL} \tag{1.10}$$

Despite $\rho = 0$ and therefore $\vec{\nabla} \cdot \vec{D} = 0$ not necessarily meaning $\vec{\nabla} \cdot \vec{E} = 0$, the factor $\vec{\nabla} \cdot (\vec{\nabla} \cdot \vec{E})$ can often be neglected. This equation can be read as a driven wave equation with the nonlinear polarization as the driver. To better understand and classify the effects caused by this source it is common to expand the polarization into a Taylor series

$$\begin{aligned} P &= \epsilon_0 (\chi^{(1)} E + \chi^{(2)} E \cdot E + \chi^{(3)} E \cdot E \cdot E + \dots) = \\ &= P_{(1)} + P_{NL} \\ P_{NL} &= \epsilon_0 (\chi^{(2)} E \cdot E + \chi^{(3)} E \cdot E \cdot E + \dots) \end{aligned} \tag{1.11}$$

This commonly used form to write out the orders of E is a reminder that this expression in the general case is a tensor equation with orientation dependent χ and the possibility of the interaction of different electric fields. Looking for example at the second order response to an electric field with two frequency components we get

$$\begin{aligned} E(t) &= \frac{1}{2}(E_1 e^{i\omega_1 t} + E_2 e^{i\omega_2 t} + cc.) \\ P_{(2)}(t) &= \epsilon_0 \chi^{(2)} E \cdot E = \\ &= \frac{1}{4} \epsilon_0 \chi^{(2)} (E_1^2 e^{i2\omega_1 t} + E_2^2 e^{i2\omega_2 t} + \\ &+ 2E_1 E_2 e^{i(\omega_1+\omega_2)t} + 2E_1 E_2^* e^{i(\omega_1-\omega_2)t} + \\ &+ E_1 E_1^* + E_2 E_2^* + cc.) \end{aligned} \tag{1.12}$$

In this all possible variations of second order frequency mixing are visible. We have second harmonic generation (SHG) with the double frequencies, sum frequency generation (SFG) and difference frequency generation (DFG), and with frequency zero optical rectification. This still is only the polarization response of the material but since it is according to equation (1.10) a source in the wave equation, light with these frequency components can be generated from it.

1.3 Optical Parametric Amplification

For some years now the classical tool for high harmonic generation and streaking applications was the Titanium:Sapphire chirped pulse amplifier seeded by a Kerr lens mode locked

laser as it routinely provides the necessary pulse energies and pulse durations. Although great progress was, and still is possible with it, among its limitations is the fixed wavelength of $\lambda_L \sim 800nm$. To be able to explore different spectral ranges new concepts are needed. While there are of course other laser materials emitting at different frequencies that are by now also used on a daily basis the most flexible concept is that of optical parametric chirped pulse amplification (OPCPA or when the chirped pulse nature is not relevant OPA). The difference here is the "parametric" part in that no real energy levels and transitions are required but the medium is only mediating the conversion process via its polarization, making it, if not material independent, much more broadband. OPA is in its core identical to the nonlinear optical process of difference frequency generation (DFG) as it is derived in the previous section 1.2. In the case of OPA not the generation of the

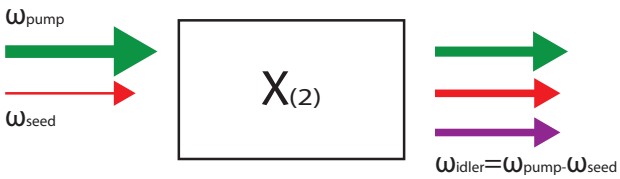

Figure 1.3: **Basic principle of OPA.** In a $\chi^{(2)}$ process the energy from the pump beam is transferred to the seed, amplifying it, and simultaneously to the newly generated difference frequency signal, the idler.

difference frequency $\omega_3 = \omega_1 - \omega_2$ is of interest but the simultaneously happening amplification of the lower frequency input ω_2, the seed. The basic setup is sketched in section 1.3. A higher frequency (higher energy), high power "pump" beam (ω_{pump}) interacts with the lower energy and power "signal" (ω_{signal}) to amplify the later. The DFG signal, the idler (ω_{idler}), is often not of interest and discarded. While the idler is not of interest for this application it is crucial for the understanding of the amplification characteristics of an OPA. Starting from equation (1.11) with

$$\begin{aligned} E_p &= A_p(z) \cdot e^{i(\omega_p t - k_p z)} \\ E_s &= A_s(z) \cdot e^{i(\omega_s t - k_s z)} \end{aligned} \tag{1.13}$$

and only looking at the DFG process term we get

$$P_i = \epsilon_0 \chi^{(2)} A_p A_s^* e^{i(\omega_i - k_i z)} \tag{1.14}$$

Inserting this into the nonlinear wave equation (1.10) it is possible to derive the coupled amplitude equations

$$\begin{aligned} \frac{dA_i}{dz} &= -\frac{i\chi^{(2)}\omega_i}{2n_i c} A_p A_s^* e^{-i\Delta k z} \\ \frac{dA_s}{dz} &= -\frac{i\chi^{(2)}\omega_s}{2n_s c} A_p A_i^* e^{-i\Delta k z} \\ \frac{dA_p}{dz} &= -\frac{i\chi^{(2)}\omega_p}{2n_p c} A_s A_i e^{i\Delta k z} \end{aligned} \tag{1.15}$$

with $\Delta k = (k_p - k_s) - k_i$ the phase mismatch. These equations are valid for the simplifying assumption of plane waves or weakly focused beams and a collinear setup but demonstrate the basic behavior. A numerical solution is plotted in section 1.3 showing for example the

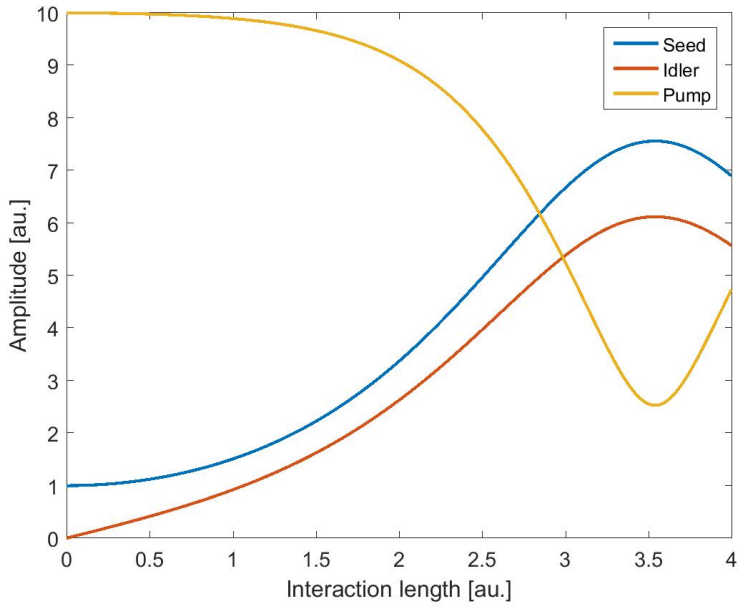

Figure 1.4: Amplitude development in an OPA with distance within a crystal. After a section of exponential signal growth pump depletion limits the gain to linear. With even stronger depletion back conversion to the pump frequency sets in.

development of the three amplitudes with distance. In a first section with unchanged pump intensity the buildup of the idler leads to an exponential growth in the signal. This is due to the symmetry of the process. While the presence of the signal causes the generation of the idler, this is also true vice versa providing positive feedback and causing an exponential increase. This symmetry is also obvious in the first two equations of (1.15). After the exponential growth the gain becomes linear due to pump depletion and at some point even reverses causing back conversion from signal and idler to the pump frequency via sum frequency generation. The strong dependence of this behavior on the input intensities is the origin of the pulse and beam distortions that are discussed later in this thesis.

1.4 High Harmonic Generation

The process of high harmonic generation (HHG) is the main topic of this thesis and always was the goal of my efforts. The challenges I encountered, especially concerning the driving laser system, limited the complexity of the investigated phenomena in a way that rather simple theories are sufficient for the understanding of most described phenomena. Although much more sophisticated theories exist, they are not necessary for the treatment of our

findings and I will limit my description here to the former.
The first observation of HHG was not in the nowadays most common medium of gases but in solids by Burnett et al. in 1977 [17]. Ten years later McPherson [15] generated the first high harmonics in gases. It then took six more years for a first intuitive, semi classical, theory by Corkum in 1993 [6] to explain many of the observed characteristics. A fully quantum mechanical description followed just one year later by Lewenstein in 1994 [18].

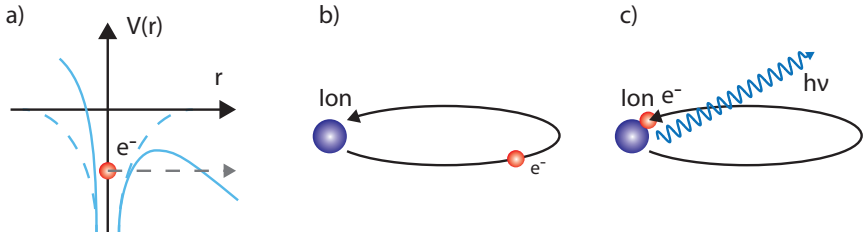

Figure 1.5: **The three step model after Corkum.** a) The electric field of the driving laser is strong enough to deform the binding potential of the electron allowing tunnel ionization. b) The assumed free electron is accelerated away from the ion by the electric field and, after it changes sign, stopped and accelerated back. c) Upon returning to the parent ion, the electron has a probability for recombination releasing the kinetic energy and the binding energy as a single XUV photon. Graph adapted from M. Fiess [19]

1.4.1 The Three Step Model

Before the explanation by Corkum [6] it was empirically found [20] that the emitted high harmonic spectrum had a limit at the high energy end at

$$\begin{aligned} E_{cutoff} &= 3.17 \cdot U_p + E_I \\ U_p &= \frac{e^2 E^2}{4m\omega^2} \end{aligned} \tag{1.16}$$

where U_p is the ponderomotive energy, E_I the ionization potential, e and m the electron charge and mass, E the amplitude of the laser electric field, and ω the laser angular frequency. Corkum's three step model, illustrated in section 1.4, could explain this finding. In a first step the electron is freed from the parent ion via tunnel ionization. The lasers electric field reaches values on the order of magnitude of the electrons' binding potential and deforms it as shown in section 1.4 a) allowing the electron to tunnel through the barrier. The electron, now treated as a free electron, is accelerated away from the parent ion by the laser's electric field (section 1.4 b). With the reversal of the sign of the electric field it is stopped and accelerated back. Upon the passing of the parent ion there is a non zero probability to recombine with it releasing the electron's kinetic energy as well as the binding potential as a high energy photon (section 1.4 c). Corkum's model calculated the kinetic energy upon recollision from the ionization probability and a classical mechanical equation of motion to be at the previously found $E_{kin} = 3.17 \cdot U_P$. Also the temporal

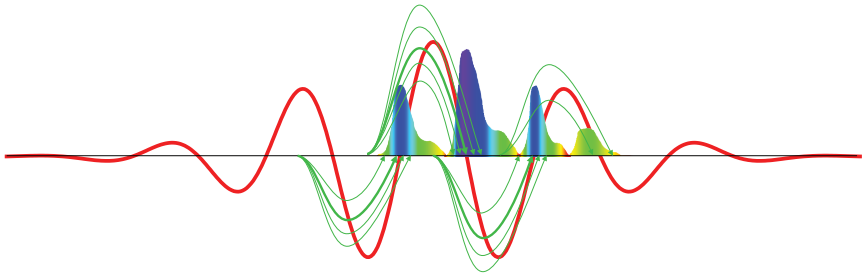

Figure 1.6: **The generation of high harmonics during the passing of a few cycle pulse.** If the necessary field strength for tunnel ionization is exceeded an XUV pulse is emitted every half cycle of the driving lasers field leading to a train of pulses. The coherent superposition of these pulses leads to the characteristically modulated XUV spectrum. *Graph by R. Kienberger*

structure of the XUV emission as a train of pulses can be explained by this model as shown in section 1.4.1. Assuming the field strength is sufficient for tunnel ionization in more than the most intense peak, the necessary conditions for the described process are fulfilled every half cycle of the driving lasers field, resulting in a train of pulses with a separation of $\Delta t = \frac{\tau_{Laser}}{2}$. This temporal structure also translates into the characteristic form of the HHG spectrum with a modulated plateau region and an unmodulated high energy cut off as can be seen in section 1.4.1. Photons in the lower energy regime are emitted at multiple cycles causing the modulated spectrum.

$$\mathcal{F}\Big\{E(t) + E(t+\Delta t)\Big\} = \mathcal{F}\Big\{E(t)\Big\} \cdot (1 + e^{i\omega\Delta t}) \tag{1.17}$$

The photons in the high energy cut off region are originating only from the one most intense cycle (section 1.4.1) leaving this part of the spectrum unmodulated.
This fact is used to isolate a single attosecond pulse from the pulse train by spectral filtering. By filtering out everything except the unmodulated cut off area only the single pulse originating from the most intense laser cycle is transmitted. This of course relies on the existence of a pronounced maximum and therefore requires laser pulse durations in the regime of only few cycles, and second, control over the CEP of the laser to adjust for a suitable waveform.

1.4.2 Wavelength Scaling

Many recent efforts in the advancement of high harmonic generation and the intention of this thesis is to shift the driving laser to longer wavelength [7, 21, 22]. The most obvious motivation for this is the scaling of the high energy cut-off of the XUV spectrum with wavelength. As mentioned earlier in section 1.4.1 this can be described by

$$E_{cutoff} = 3.17 \cdot U_p + E_I \propto I\lambda^2 \tag{1.18}$$

While in this equation the I is limited by ionization levels preventing phase matching (section 1.4.3) and the used laser systems, a change in the wavelength is a possibility

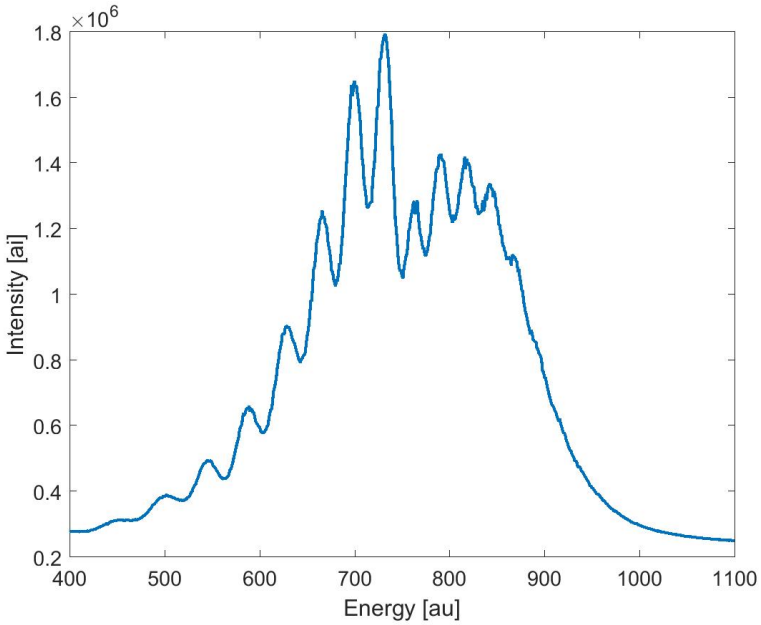

Figure 1.7: Sample XUV spectrum with pronounced modulations and unmodulated high energy cut off region. The decreasing intensity in the low energy region is caused by a zirconium filter (compare section 3.1.3) in the beam.

to achieve cut-off energies that were previously unreachable. The shift to higher photon energies however comes with a price, the conversion efficiency decreases significantly. Numerical calculations by Tate et al. [23] gave a $\propto \lambda^{-5.5\pm0.5}$ dependence. Experimental data by Shiner at al. [24] even suggests $\lambda^{-6.3\pm1.1}$ for the generation in Xe and $\lambda^{-6.1\pm1.1}$ in Kr. From that a factor of λ^{-3} can be explained by the increasing spread of the electron wave packet in space and time due to the longer trajectories with increasing wavelength. For a fixed XUV energy range an additional factor of λ^{-2} is due to the quadratic extension of the spectrum [25]. This very unfavorable scaling suggests the use of new schemes of phase matching to at least partially compensate for it.

1.4.3 Phase Matching

The previously described three step model is an atomic description of the process of HHG. It is explaining the underlying mechanism but for an experimental implementation that is not sufficient. To generate measurable and later on usable amounts of XUV it is necessary that the process takes place in a macroscopic volume, in a large number of atoms and their output is adding up constructively. The generation needs to happen in phase over an extended distance. Section 1.4.3 illustrates the principle for the case of second harmonic generation. In a) the generating (blue) and generated (red) field have a constant phase relation $\Delta k = 0$ leading to a constructive buildup. In b) with unmatched phase velocities the buildup only happens over the distance it takes to generate a phase slip of $\Delta\phi = \pi$,

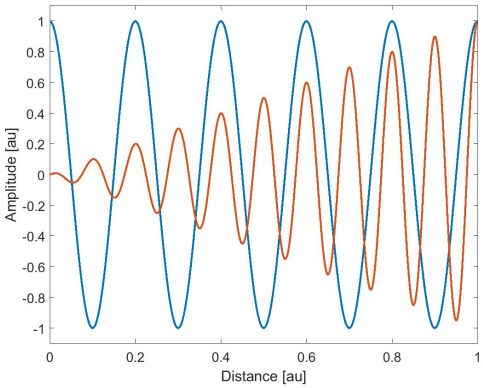

(a) Ideal phase matching $\Delta k = 0$ leads to a linear increase in the generated field

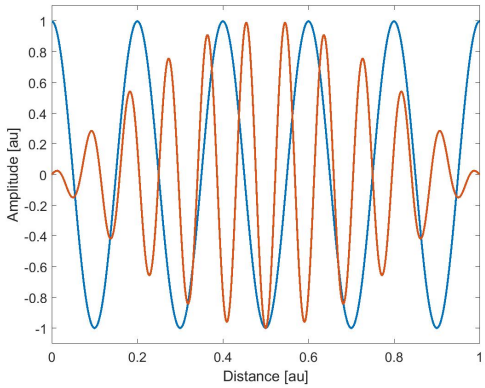

(b) A phase mismatch shifts the phase relation between generating and generated field leading to destructive interference and a decrease in the generated field.

Figure 1.8: Illustration of ideal phase matching vs. the effect of a phase mismatch in the case of second harmonic generation.

the coherence length $L_{coh} = \frac{\pi}{\Delta k}$. After that the generated amplitude decreases again. In the case of perturbative effects, often birefringence of the nonlinear medium is exploited to match the refractive indices of the involved fields and achieve $\Delta k = 0$. Since HHG as discussed in this thesis takes place in a gas this is not possible. Accessible parameters here are the gas density, the intensity of the driving laser and with that the degree of ionization in the gas, and the geometry of the HHG setup. To discuss phase matching for high harmonic generation, one additional result from Lewensteins theory [18] is necessary. On its trajectory the electron is acquiring a quantum phase, dependent on the intensity of the driving laser, that is transferred to the emitted photon and therefore needs to be considered in phase matching.[26] Due to its intensity dependence this factor is to some extent accessible via the geometry of the experiment.

Tight Focusing

In the tight focusing geometry the beam is focused into a short gas target as shown in section 1.4.3. For this geometry Balcou et al. [26] could show that collinear phase matching can be achieved placing the gas target slightly after the focus position (position a in section 1.4.3). At that position the decrease in quantum phase of the XUV caused by the decreasing intensity of the driving laser is matched with the Gouy phase the driving laser acquires passing the focus. For positions in front of the target on axis (c in section 1.4.3) these two contributions have opposite sign leading to rapid oscillations in the phase making phase matching impossible. For off-axis positions however phase matching is possible leading to a diverging annular emission. Since this emission is hard to use in an experimental setup this is rather of academic interest. Balcou [26] neglects dispersive effects caused by

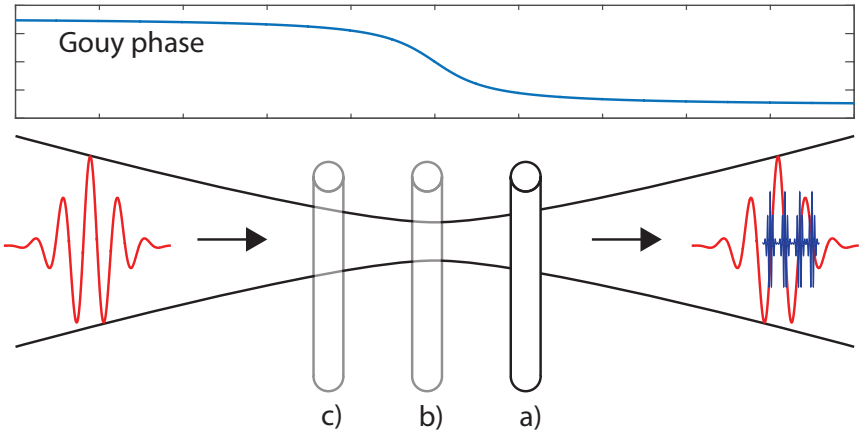

Figure 1.9: Tight focusing geometry for high harmonic generation. The laser is focused into a short gas target. Calculations show that collinear on axis phase matching is achievable shortly after the focus (position a). At that position the change in the intensity dependent quantum phase is matched with the behavior of the Gouy phase.

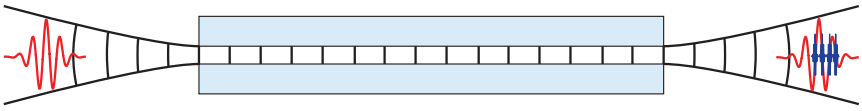

Figure 1.10: Wave guide geometry for high harmonic generation. The beam is focused into a hollow core fiber (HCF) enforcing plane wave geometry over the distance of the fiber.

the neutral and ionized gas, looking only at geometric effects. These can however easily be included in the phase matching scheme. In total, contributions to the phase are neutral gas and plasma dispersion, Gouy phase, and quantum phase. Experimental implementations usually vary the target position, the gas pressure, and the laser intensity to find a balance between these contributions.

Hollow Wave Guide

A different approach to phase matching in HHG is displayed in section 1.4.3. The idea is to use a hollow gas filled wave guide to get plane wave geometry over an extended distance, avoiding phase and intensity effects by the expanding beam. In this configuration a new factor becomes relevant for the phase matching considerations, dispersion of the wave guide. Although a hollow (approximately non-dispersive) waveguide is used, the guiding by the cladding leads to contributions that need to be considered. With that the phase mismatch reads as [27]:

$$\begin{aligned}\Delta k(t) &= k_{q\omega} - q k_{\omega} = \\ &= q\left\{\frac{u_{11}^2 \lambda_L}{4\pi a^2} - P\left([1-\eta(t)]\frac{2\pi}{\lambda_L}\delta n - \eta(t) N_{atm} r_e \lambda_L\right)\right\} + \Delta k_{quantum}(t)\end{aligned} \tag{1.19}$$

with q the harmonic order, u_{11} the lowest order waveguide mode factor, λ_L the central wavelength of the driving laser, a the inner radius of the waveguide, P the gas pressure, η the ionization fraction, δn the difference in the refractive index of the fundamental and the q-th harmonic, N_{atm} the number density of the gas at one atmosphere pressure, r_e the classical electron radius, and $\Delta k_{quantum}$ the quantum phase. In this equation the first term is accounting for the waveguide dispersion. It is assumed that only the driving laser will interact with the waveguide while the generated harmonic beam is so small that it will remain fully in the hollow core. The first pressure-dependent term is the neutral gas dispersion accounting for the difference in the refractive index of the different wavelengths. The second pressure dependent term is the plasma dispersion. The temporal dependence describes that phase matching will usually only be achieved on the timescale of the pulse when the generated plasma density in combination with suitable pressure and intensity values leads to $\Delta k(t) = 0$. Equation (1.19) also makes clear that there exists a critical ionization fraction that if exceeded prevents phase matching. The pressure dependent term is the only part of the equation able to contribute a negative factor which is necessary to get $\Delta k = 0$. Setting this to zero to get an upper limit one obtains

$$\eta_{cr} = \left(1 + \frac{N_{atm} r_e \lambda_L^2}{2\pi\delta n}\right)^{-1} \tag{1.20}$$

This limit is valid for plane wave geometries like in wave guides or gas cells (section 1.4.3). In the case of tight focusing (section 1.4.3) the Gouy phase is an additional contribution softening that limit.

Gas Cell

Just for completeness I want to mention the possibility of a quasi plane wave geometry in an extended gas cell. Especially for lasers with very high pulse energies like for example LWS20 [28] large foci are necessary to avoid too high ionization levels. The required long focusing leads to close to plane wave propagation for an extended distance. The phase matching condition then is very similar to that of equation (1.19) except without the geometric term. Since this requires pulse energies far exceeding ours it was not used during this thesis.

1.5 Attosecond Streaking

Attosecond streaking is an extension of the concept of streak cameras as they have been used routinely for decades to characterize short pulses. Both ideas have the common concept of the generation of free electrons with an optical pulse in a suitable medium and their subsequent time dependent acceleration by an electric field. In both cases the resulting distribution of the electrons allows the characterization of the pulses by mapping time onto another observable such as position or energy.
The technique became possible and started to evolve with the generation and isolation

of single attosecond pulses[16]. The most common setup is to use HHG as described previously to generate a single isolated attosecond pulse that is intrinsically synchronized with the driving laser pulse. It is now possible to adjust the temporal delay between the pulses on a sub-femtosecond timescale. The beams are finally spatially recombined in a common focus. Putting a suitable medium at that focus position it is possible to generate free electrons via ionization with the XUV pulse. Due to the attosecond duration of the XUV pulses the emission of the electrons is confined to the same timescale.

Usually the integral over the electric field of an optical pulse is zero $\int_{-\infty}^{\infty} E(t)dt = 0$. This means that an electron will not experience any resulting change in its momentum after the pulse has passed. Because we are now in the position to free the electrons during the passing of the pulse this changes. In a classical picture the electron experiences a change in momentum according to

$$\Delta p = e \int_{t_0}^{\infty} E_L(t)dt = eA_L(t_0) \tag{1.21}$$

with Δp the change in momentum, $E_L(t)$ the lasers electric field and $A_L(t)$ the lasers vector potential. With the electrons initial momentum narrowly defined by the combination of the XUV pulses energy and the ionization potential of the used medium this allows the complete characterization of the driving laser pulse [29]. Section 1.5 demonstrates the

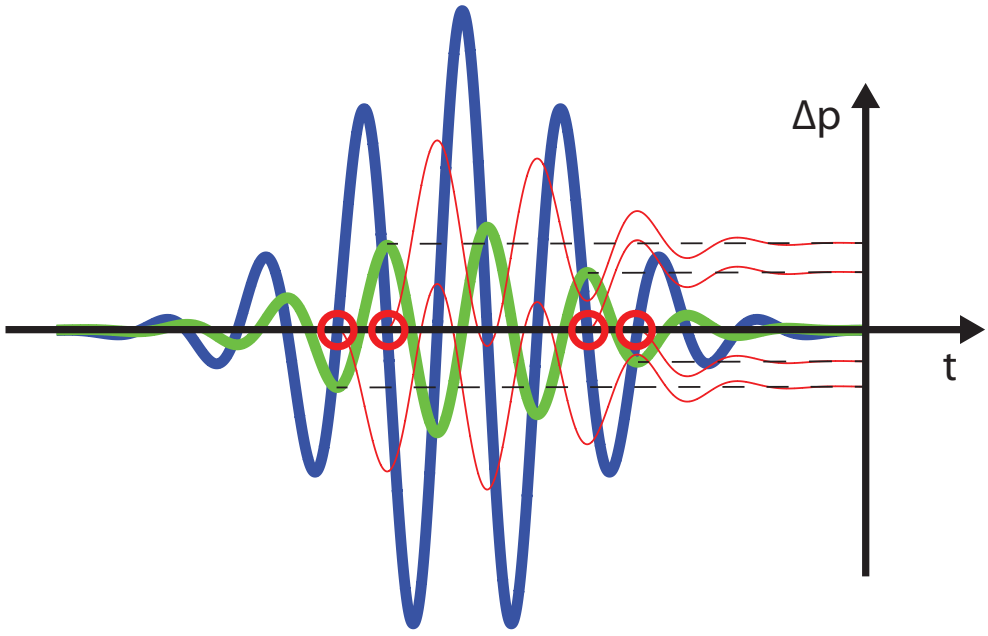

Figure 1.11: Principle of attosecond streaking. Free electrons are generated by an XUV pulse at different adjustable times (red circles). They are accelerated by the passing laser pulse (blue) and end up with a change in momentum proportional to the vector potential (green) at the time of their generation. *Adapted from R. Kienberger*

principle. Free electrons are generated at different times (red circles) during the passing of

the pulse (blue). The electrons are accelerated by the electric field of the pulse and end up with a change in momentum depending on their "time of birth" proportional to the vector potential (green) of the laser pulse.

The model shown here of course is a strong simplification. The resulting spectrogram in detail is a convolution of all involved processes. This includes: The characteristics of the XUV pulse which is not a temporal delta function with a single energy, the process of the emission of photo-electrons which, depending on the medium, can result in a whole spectrum of possible energies, and the interaction of the electron wave packet with the lasers field. FROG (Frequency Resolved Optical Gating) like reconstruction algorithms can be used to characterize the XUV as well as the IR pulse from the resulting spectrogram [30] [31]. Section 1.5 shows for example simulated streaking spectrograms from an XUV

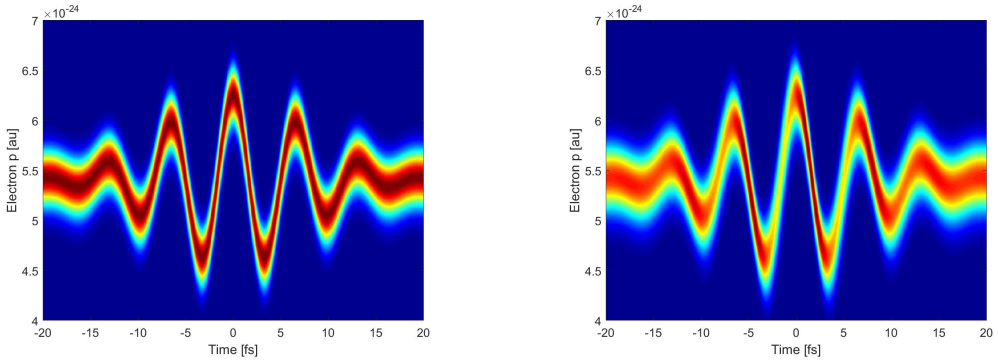

(a) Unchirped XUV pulse

(b) Chirped XUV pulse

Figure 1.12: Simulated streaking spectrograms of an XUV pulse with a central energy of 100 eV and 20 eV bandwidth and a $\lambda = 2\ \mu m$ streaking pulse.

pulse with 100 eV central energy and 20 eV bandwidth in combination with a $\lambda = 2\ \mu m$ streaking pulse. It is assumed that no additional phase, time dependence, or energy is acquired by the electrons during emission. In a) the XUV pulse with a FWHM duration of 160 as has a flat phase resulting in a "featureless" streaking trace. A chirp of the XUV pulse of $GDD = -2 \cdot 10^4\ as^2$ in b) changes the duration to 400 as and the trace to have different characteristics for the rising and the falling flank of the IR pulse. The result of a XUV pulse with a bandwidth of only 2 eV and an according pulse duration of 1550 as is depicted in section 1.5. The IR streaking amplitude was reduced proportionally to the bandwidth to one tenth. Here the long pulse duration leads to significantly weaker flanks opposed to the peak positions.

An even more detailed analysis also enables the measurement of the quantum phase associated with the transition from bound to continuum states during ionization [32]. During this thesis only the characterization of the involved pulses was of interest.

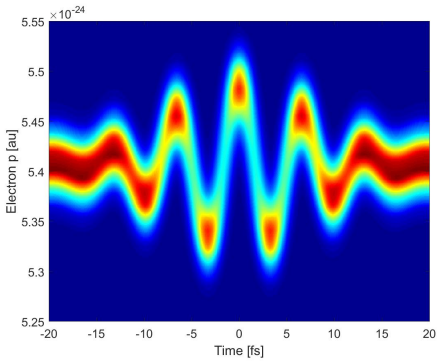

Figure 1.13: Simulated streaking spectrograms of an XUV pulse with a central energy of 100 eV and 2 eV bandwidth and a $\lambda = 2\ \mu m$ streaking pulse.

Chapter 2

Laser System

2.1 Basic Setup

The system used for performing the work described in this thesis is the "Light Wave Synthesizer 1" (LWS 1) in the Laboratory for Attosecond Physics at the Max Planck Institute of Quantum Optics (MPQ). It is a three stage OPCPA (Optical Parametric Chirped Pulse Amplifier) operating at a central wavelength of 2 μm with pulse energies of 1 mJ and pulse durations of 18 fs. Most of my description of the system will be very brief. For more details of the initial design see the PhD thesis of Alexander Schwarz [33]. A more in depth description will only be made for changes that were necessary for the experiments that are the topic of this thesis.
The common front end for seed generation as well as the pump chain consists of a commercial Femtolasers[1] Rainbow II Titanium Sapphire oscillator. (Section 2.1) This common source ensures an intrinsic temporal synchronization between pump and seed pulses.

2.1.1 Seed Generation

The front end oscillator is seeding a commercial Titanium Sapphire CPA (Femtolasers Femtopower Pro) producing 1 mJ pulses at 800 nm with a duration of 23 fs. 10 % of the pulse energy is used for the seed generation and broadened in a Krypton filled hollow core fiber, subsequently compressed with a chirped mirror compressor to 4 fs duration. Via intrapulse difference frequency generation (DFG) in BBO the seed spectrum (Section 2.1.1) centered at 2 μm is generated. A big advantage of the seed generation via DFG for the purpose of this system is the intrinsic CEP stability resulting from it. Since CEP stability is crucial for most intended applications this saves complicated active stabilization setups.

A dichroic beam splitter is separating the IR seed from the remaining white light which is reused as the probe for the pulse characterization technique 'Electro optic sampling' (EOS).

[1] Now Spectra-Physics Vienna `https://www.spectra-physics.com/company/vienna`

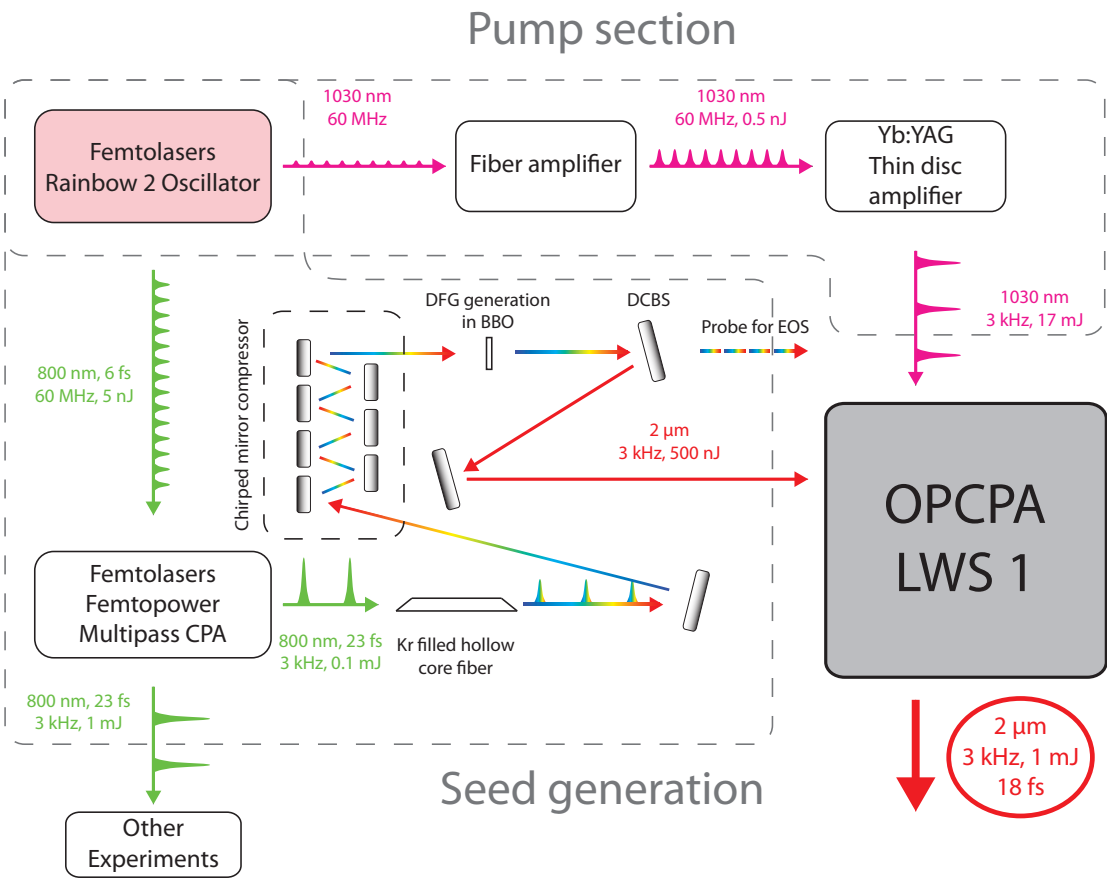

Figure 2.1: **Seed generation and pump of LWS1**. A commercial Ti:Sa CPA seeded by a Ti:Sa oscillator followed by spectral broadening and DFG generates the seed. An Yb:YAG regenerative amplifier seeded by the same oscillator generates the pump. The common source of both paths ensures intrinsic temporal synchronization. For the OPA setup see section 2.1.3

2.1.2 Pump Generation

The Femtopower Rainbow 2 oscillator is specially modified to also have frequency components at 1030 nm which are generating an IR pulse train intrinsically synchronized with the seed chain originating from the usual 800 nm output of the oscillator. These pulses are passing through a pre amplification stage consisting of a fiber amplifier (Tünnermann group, Friedrich-Schiller-Universität Jena) increasing pulse energies to 0.4 nJ. The amplified pulses are used to seed the main pump laser, an Ytterbium doped Yttrium Aluminum Garnet (Yb:YAG) thin disk regenerative amplifier [34]. After compression in a reflective grating compressor the output pulse parameters are 3 $kHz, 1.2\ ps, 17\ mJ$.

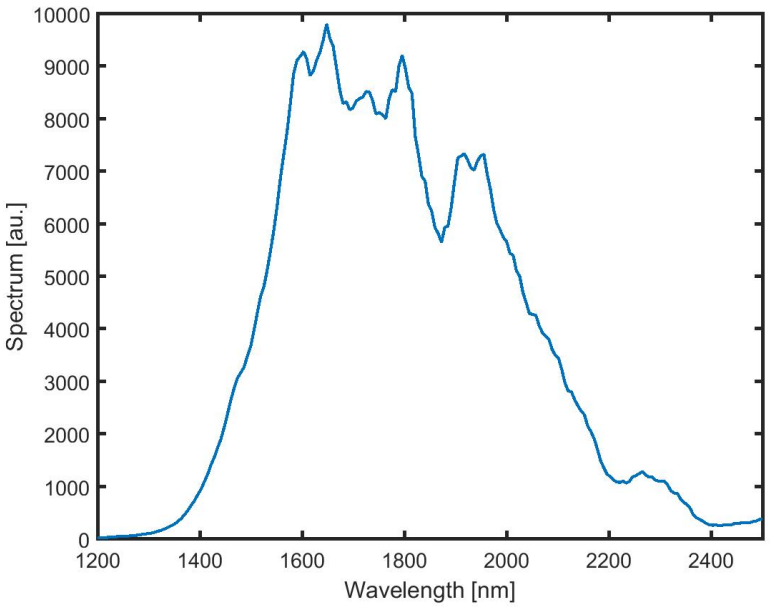

Figure 2.2: LWS Seed Spectrum generated in BBO

2.1.3 OPCPA Setup

The OPCPA consists of three stages amplifying the seed step wise from pulse energy levels in the regime of nJ to the regime of 1 mJ (Section 2.1.3). Though pump and seed are originating from the same source, the Rainbow oscillator, and are therefore synchronized, an active temporal stabilization based on a TEM Aligna system[2] is employed to compensate for jitter originating from mechanical sources [35]. An Acousto-Optic Programmable Dispersive Filter(AOPDF) (Fastlite[3] Dazzler) is used to control dispersion and precompensate the accumulated phase in the OPA to allow for optimal compression. Additionally, to optimize transmission through the AOPDF by fitting the optical pulse duration to the duration of the Dazzler transmission window, 9 mm of bulk Si are used.

2.1.3.1 Optical Materials

First and second stage are using Periodically Poled Lithium Niobate (PPLN) as amplification media increasing pulse energies to 8.5 μJ and 85 μJ respectively. Due to the limited damage thresholds of PPLN and the limited maximum aperture PPLN can be manufactured in the third stage can not be operated with the same medium. Initial designs[33] were using bulk Lithium Niobate ($LiNbO_3$) which aside from the intended amplification also generated the second harmonic of the signal wasting significant amounts of usable energy. The efficiency could be improved by a novel design using a “hybrid” stage consisting

[2] http://www.tem-messtechnik.de/EN/aligna.htm
[3] http://www.fastlite.com

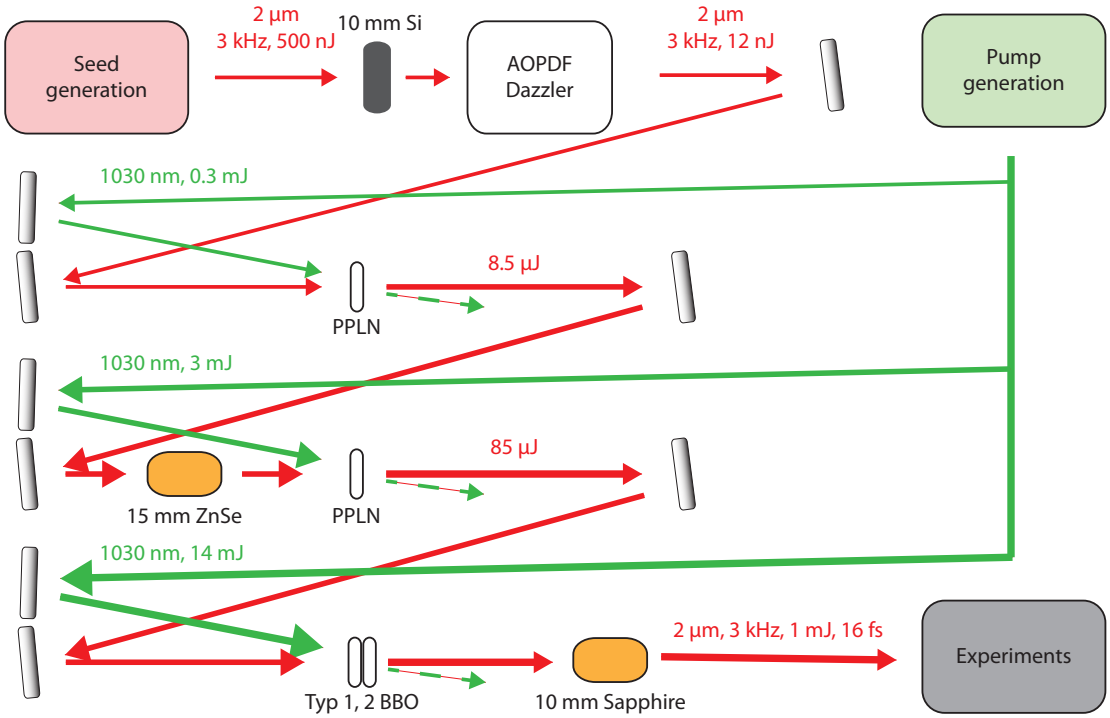

Figure 2.3: Basic setup of LWS1.

of two Beta Barium Borate (BBO) crystals, one type I, one type II, stacked immediately behind each other. By the combination of the amplification regimes of the two different crystals similar bandwidth as with bulk LNB can be achieved while having the larger damage threshold as well as the larger possible apertures of BBO (Section 2.1.3.1a). Looking at the amplified spectra after the respective stages a clear difference between the two materials can be seen. Section 2.1.3.1b is showing the amplified spectra after all three stages normalized to the respective total power. While the spectra from stages one and two look fairly similar the change in the spectrum caused by the third stage is clearly visible. Still, the bandwidth is very similar preserving the possibility for the same short pulse durations.

2.1.3.2 Chirp Control and Compression

Initial stretching of the pulses is performed by the AOPDF. Unintuitively, it is beneficial to first add opposite sign, positive chirp via the 9 *mm* Si in front of the device to optimize transmission by increasing the length of the acoustic waveform required to obtain a short pulse at the end of the system. Then the chirp is reversed within the Dazzler resulting in a negatively chirped pulse beneficial to amplification in PPLN in the first two stages. As on the other hand a positive chirp is beneficial for amplification in BBO, the third stage, the chirp is reversed by 15 *mm* of bulk ZnSe. In the initial installment of this pattern the chirp reversal was put in the intuitively right position between second and third stage. At that position however the already significant pulse energy in combination with the fact

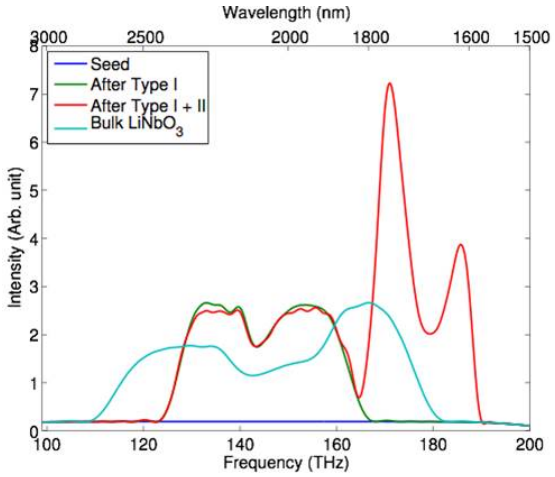

(a) Theoretical comparison of the amplification in bulk $LiNbO_3$ vs. stacked BBO crystals. The combination of type I and type II BBO results in an amplification spectrum that is slightly blue shifted but has similar bandwidth as $LiNbO_3$.

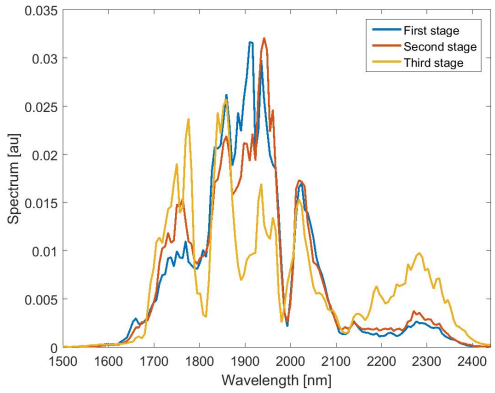

(b) Normalized spectra after first, second, and third stage of the OPCPA. While first and second stage are similar a clear difference caused by the different type of OPA crystal for third stage can be seen, although with similar bandwidth.

Figure 2.4: Comparison of the amplification in $LiNbO_3$ vs. stacked BBO crystals.

that the pulse is compressed within the ZnSe led to clearly visible Kerr lensing[36]. The resulting intensity dependent focusing geometry of the third stage caused problems on long as well as short time scales. Small, fast fluctuations in the output of the second stage were amplified by the changing geometry. Slow, small drifts in power of the second stage significantly changed the output of third stage as well as the beam divergence after the OPA causing serious problems in the application of the generated beam. The solution to the described problems was to put the ZnSe between the first and second stage. Since the chirp in this configuration now has the wrong sign for the second stage this is of course a tradeoff resulting in less amplification in the second stage. The stability after the third stage however improved significantly. The total loss in power by this configuration is hard to quantify. Since the previous output was temporally very unstable the loss in usable power probably is negligible.

2.2 Stability Improvement by Chirp Reversal between Stages

An additional benefit of reversing the chirp between OPCPA stages beside fitting the chirp to the OPA crystal materials is improved stability against temporal jitter between pump and seed. In a conventional setup with constant chirp direction a temporal shift between pump and seed will lead to a spectral shift increased in each stage. Reversing the chirp between the stages leads to an opposite sign of the effect in the next stage decreasing

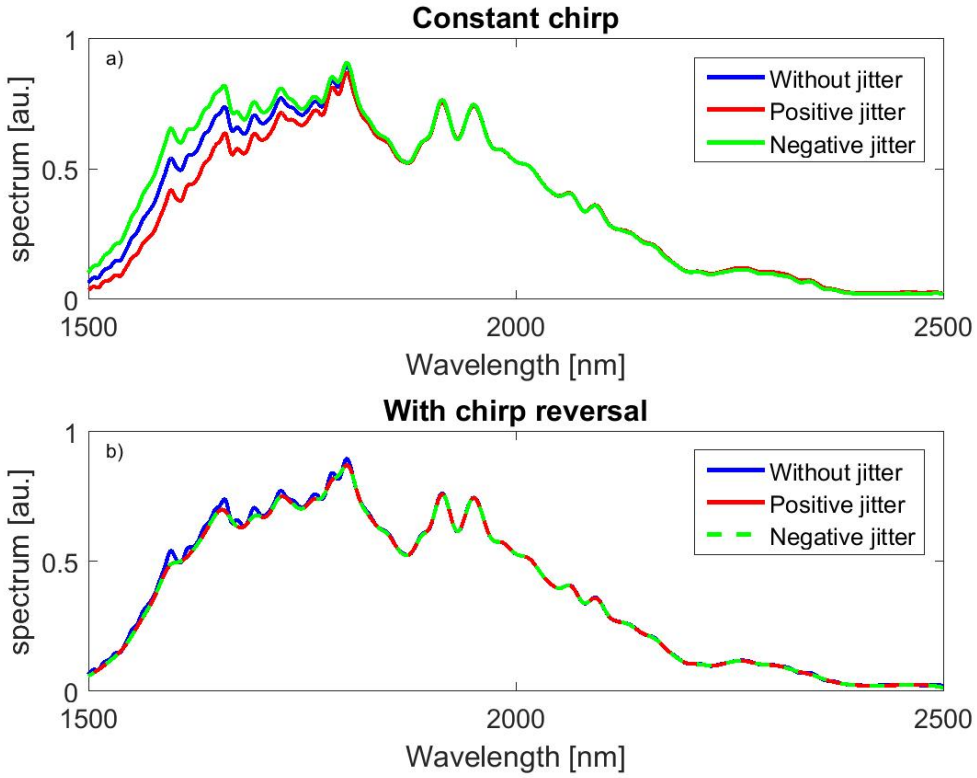

Figure 2.5: **Model calculation of the effect of chirp reversal between OPCPA stages on stability against temporal jitter.** Spectra after amplification in two consecutive identical stages with and without a $\pm 50\ fs$ shift of the pump window. a) Without chirp reversal in between. b) With chirp reversal between stages. A significant difference in the resulting spectrum for a positive and a negative time shift can be seen in a). For the case of the reversed chirp in b) the difference is almost negligible meaning an improvement in stability against temporal jitter.

the overall impact. A simple model calculation shown in section 2.2 is demonstrating the effect. Assuming amplification in two consecutive identical stages the resulting spectra are plotted. The calculation is assuming an identical t^4 supergaussian amplification profile with a full width half maximum of 1 ps in both stages. The seed pulse is stretched with a GDD of $2000 fs^2$ and in the second case reversed to $-2000 fs^2$. The temporal deviation used is $\Delta t = \pm 50\ fs$. a) is showing the case of constant chirp, b) the case of chirp reversal between stages. In both cases the undisturbed spectrum as well as the spectra with positive and negative temporal deviation are shown. While in the first case a clear difference in the resulting spectra between positive and negative temporal deviation is visible it is negligible in the second case which means an improvement in shot to shot stability in the presence of temporal jitter.

Chapter 3

Experimental Setup and Supporting Simulations

3.1 Beamline Layout

The requirements for attosecond experiments using high harmonic generation (HHG) are high. Due to the necessary intensities, the resulting nonlinearities, and the fragility of pulse compression against dispersion as well as absorption in ambient air, vacuum is a necessity. The inaccessibility of experimental setups in vacuum makes motorization crucial. The AS4 beamline at the Max-Plack-Institute of Quantum Optics was built specifically for the purpose of attosecond experiments, including streaking, in the near IR addressing these requirements. The status of the setup described in this chapter is a brief overview of the final version that was used for the attosecond streaking experiments described later. Different versions and intermediate attempts will be described separately.

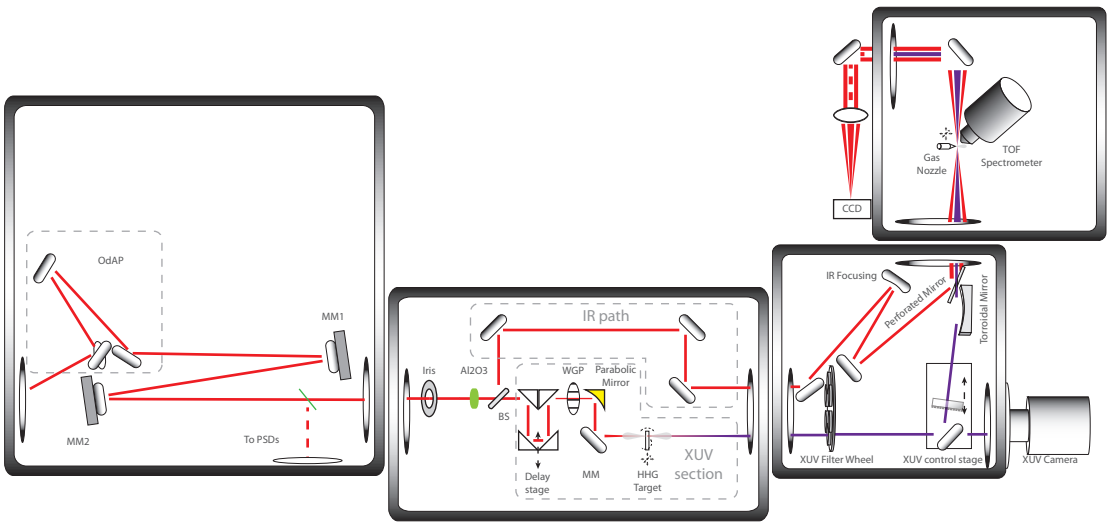

Figure 3.1: Setup of the AS4 Beamline at the Max-Planck-Institute of Quantum Optics.

Section 3.1 shows the general setup of the beamline. It consists of four different separable chambers. All sections as well as the beam guide from the laser (chapter 2) are pumped in a two stage setup consisting of a 10^{-1} $mbar$ pre-vacuum with consecutive turbo pumps bringing pressures (without gas load from the HHG target) to 10^{-6} $mbar$, 10^{-8} $mbar$ in the streaking chamber. The overall vacuum quality during operation (with gas load) is improved by differential pumping confining the system inherent high pressures mostly to the respective chamber. The individual chambers of the beamline can be distinguished by function.

3.1.1 Beam Preparation

The preparation chamber (section 3.1.1) is the first chamber of the setup. The beamline is located one floor below the laser making an elaborate beam guide necessary. Due to the floor plan of the building and existing previous installations this means a beam path of 12 m with five intermediate mirrors including an odd angle periscope. As the periscope is rotating the polarization to an inconvenient direction an additional compensating odd angle periscope (OdAP in section 3.1.1) is installed.

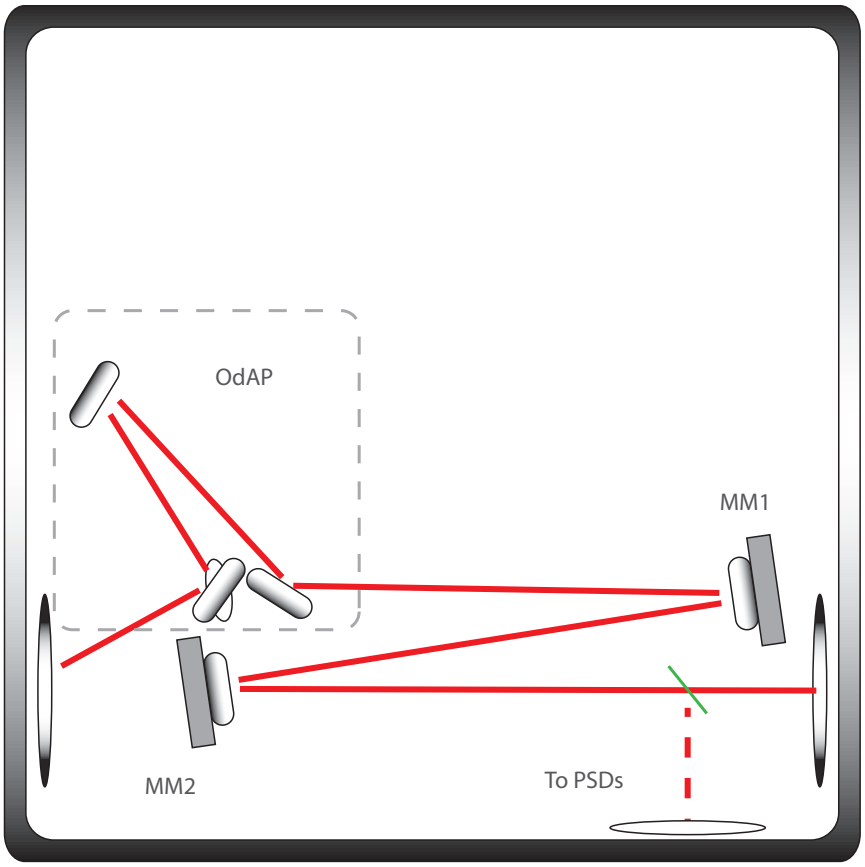

Figure 3.2: Polarization correction and beam stabilization

The long distance from the laser to the experiment causes even small vibrations from running devices (e.g. pumps, cooling fans) to have a noticeable effect on beam stability and the stability of experiments. To counter these effect we are using a TEM Aligna 4D beam stabilization system[1]. It consists of two Position Sensitive Diodes (PSDs) for detection of the current beam position and direction as well as two motorized mirrors (MM1 and MM2 in section 3.1.1) to compensate deviations from the desired status. The motorization includes stepper motors for the compensation of large scale, slow drifts and piezo actuators for fast, small vibrations. The detection signal is split off of the main beam using a nitrocellulose pellicle beam splitter (to PSDs in section 3.1.1).

3.1.2 High Harmonic Generation

The high harmonic chamber (section 3.1.2) is the main chamber of the experiments performed during this thesis.

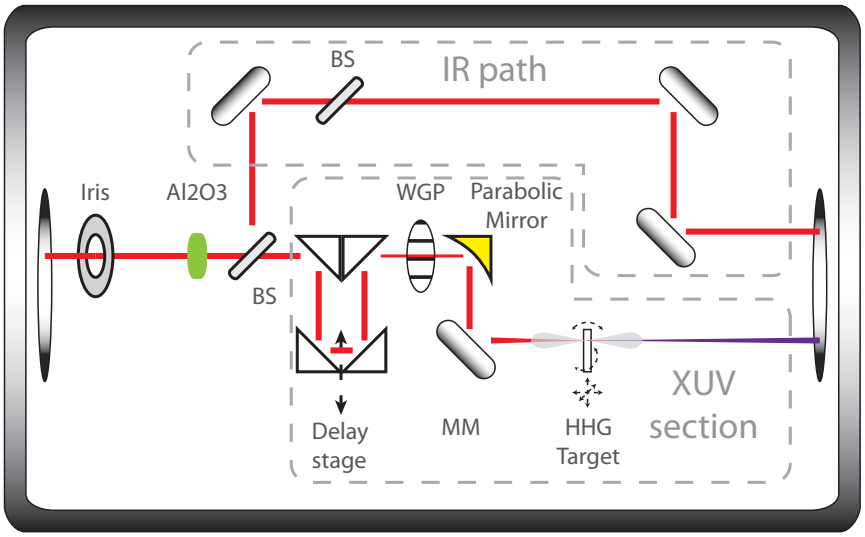

Figure 3.3: High harmonic generation and IR split off

A motorized iris at the entrance of the chamber is used for mode cleaning as well as the control of the intensity in the HHG target. A 10 mm piece of Al_2O_3 (Al2O3 in section 3.1.2) is the final dedicated element for pulse compression. The idea behind the decision to put it at this location is to avoid a compressed pulse as long as possible to avoid unwanted nonlinear effects. Before compression here the pulse has a full width half maximum of around 100 fs (calculated) compared to compressed durations of 16 fs (measured with EOS and FROG) reducing the peak intensity significantly.
To maintain a better pulse and beam quality unaffected by the highly nonlinear process of HHG the IR streaking field is split off here using a SiO_2 beam splitter (BS in section 3.1.2). The resulting difference in dispersion between the IR and the HHG arm is compensated

[1] `http://www.tem-messtechnik.de/EN/aligna.htm`

by a following identical piece of SiO_2. The following delay stage is necessary to control the temporal overlap of the HHG and the IR arm for the streaking experiments described later.
The sensitivity of the HHG process to deviations from linear polarization lead to the placement of a wire grid polarizer (WGP in section 3.1.2) cleaning the beam of detrimental components right before the focusing gold parabola. A motorized mirror (MM) enables beam pointing control without affecting the sensitive alignment of the focusing parabolic mirror.
The HHG target mount is translatable in all three spatial dimensions as well as rotatable around the two axes perpendicular to the beam axis. This enables optimal placement of the target in the focus without the necessity to move the beam.

3.1.3 XUV Diagnostics and Control

Following the generation of the attosecond pulse train is a section for XUV diagnostics and control of the XUV beam (section 3.1.3).

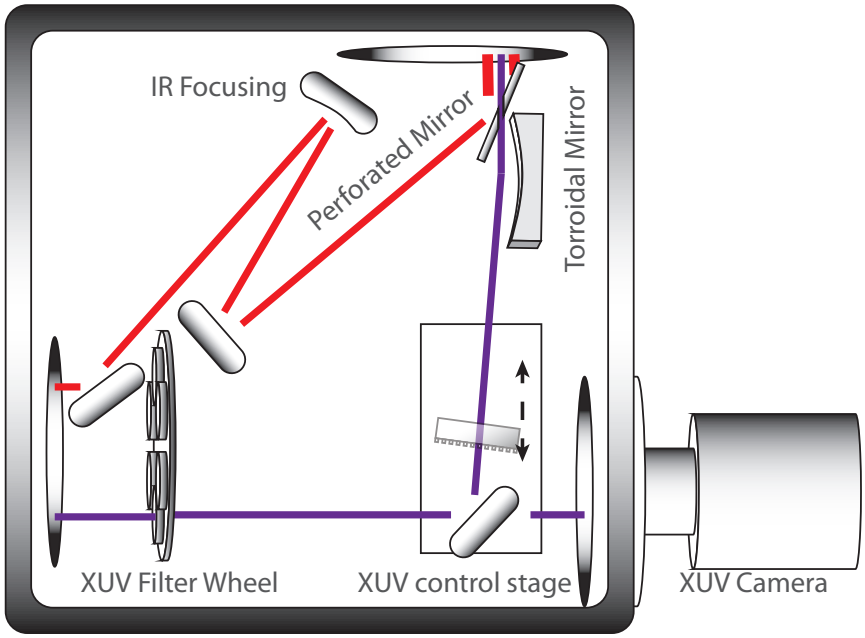

Figure 3.4: XUV diagnostics, focusing and steering

The beam is passing a filter wheel containing thin metal filters used to suppress the remaining IR as well as for spectral filtering of the XUV pulse train. In use are zirconium with a broad, flat transmitted spectrum for IR suppression as well as aluminum, silicon and boron with sharp absorption edges for energy calibration (section 3.1.3).

The main diagnostics tool is a Princeton Instruments PIXIS-XO 400 XUV camera. The camera is used in different configurations. Without additional components the beam mode can be imaged and its position recorded. Using the “XUV control stage” (section 3.1.3)

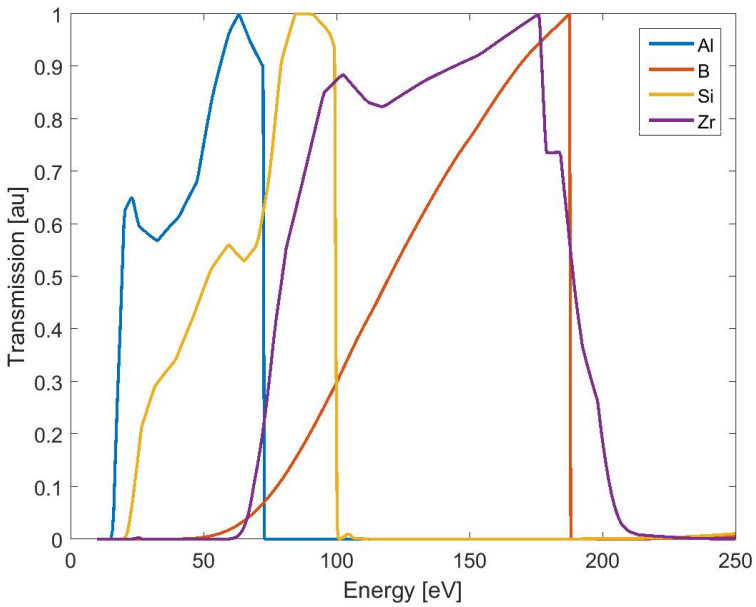

Figure 3.5: Normalized transmission spectra of the used XUV metal filters

a Hitachi 001-0266 [37] focusing grating can be inserted into the beam path enabling the recording of the XUV spectrum. For the energy calibration of this spectrometer the previously mentioned metal filters (Al, Si, B) are used. The "XUV control stage" (section 3.1.3) also contains an XUV multilayer mirror to send the beam to the streaking experiment.
For the streaking experiment the chamber contains the focusing as well as the collinear recombination of both beams. The IR beam is focused using a spherical mirror and reflected off the surface of a perforated mirror. The XUV is focused using a toroidal mirror and passes through the hole in the perforated mirror. After this, the beams are collinear with matching divergence to have overlapping foci.

3.1.4 Streaking

The final chamber of the beamline is the experimental chamber designed to perform attosecond streaking measurements. For this it is equipped with a time of flight (ToF) electron spectrometer (Kaesdorf ETF11 [2]) mounted with the entrance opening in the vicinity of the common focus of IR and XUV. We are performing the streaking measurements in neon. The gas nozzle to deliver it to the focus is mounted translatable in all three directions to make optimal positioning possible. To make positioning easier the focus is imaged onto a CCD camera on the outside of the chamber.
The ToF uses a multi channel plate (MCP) for the detection of the individual electrons making the requirements for the vacuum quality in this chamber higher than in the rest

[2] `https://www.kaesdorf.de`

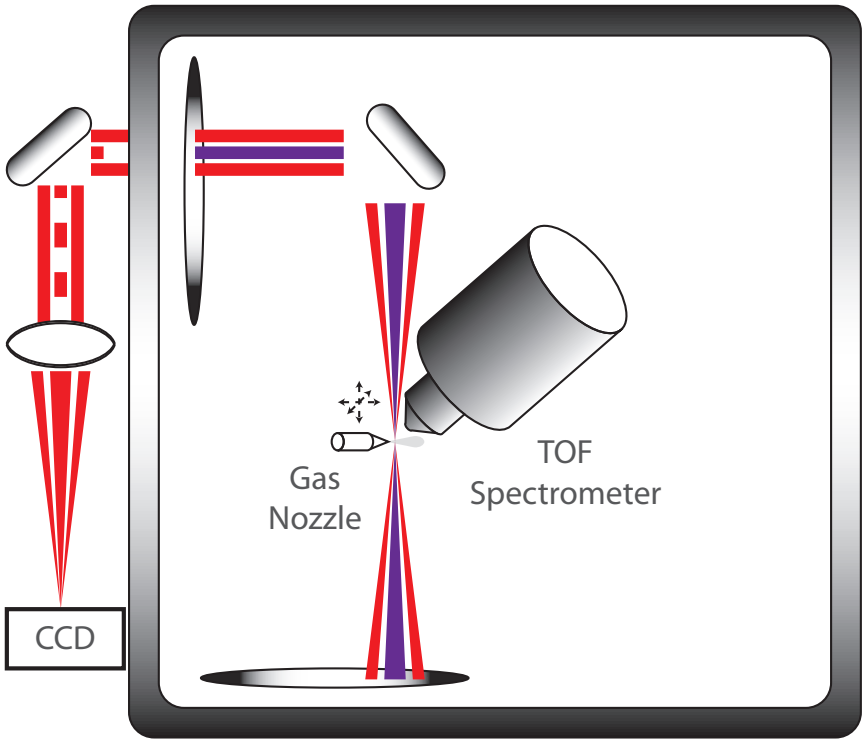

Figure 3.6: Streaking chamber layout

of the beamline. On one hand the working principle of a multi channel plate with its high voltage limits the maximum possible pressure during operation. On the other hand, since signal quality for the measurements linearly depends on the number of detectable electrons and therefore the neon density at the focus position, all avoided background pressure improves signal quality. To achieve this the chamber is designed for ultra-high vacuum (UHV) with ConFlat (CF) components with the feedthrough to the adjacent chamber as small as possible. With this we achieve background pressures with running beamline operations of $p = 2 \cdot 10^{-7}$ $mbar$ at the MCP, $\sim$ 10 % of the maximum pressure of $\sim 2 \cdot 10^{-6}$ $mbar$ restricting the possible neon pressure only slightly.

3.2 Target Designs

3.2.1 Waveguide Targets

There are a few different common designs for high harmonic gas targets driven by different phase matching schemes [27]. The initial idea for this thesis was the design of a gas filled hollow core fiber as it is sketched in section 1.4.3. The mode cleaning effect of a HCF and the much longer phase matching distance in comparison with a tight focusing geometry (section 1.4.3) promises a significant increase in conversion efficiency to compensate for the atomic wavelength scaling (section 1.4.2). The expected high gas pressures [38] lead

to the design of a steel gas cell with a V-groove to hold the actual fiber. Section 3.2.1

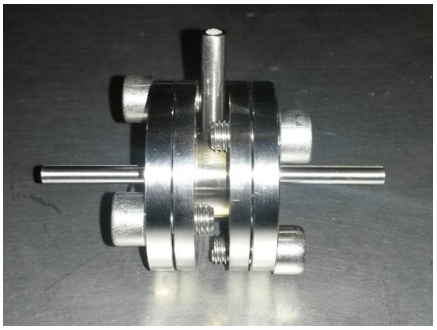

(a) Short version

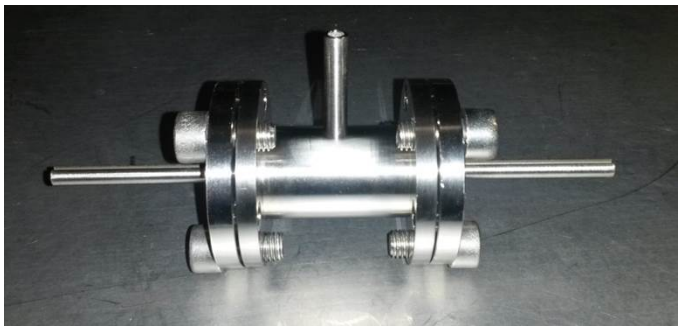

(b) Long version

(c) V-groove with flanges.

(d) Fiber with drilling holes for gas access.

Figure 3.7: a), b) Steel gas cells in different length versions. c) V-groove to hold the hollow core fibers for wave guiding and harmonic generation. The cells with the grooves are designed to withstand the pressure of several bar. d) Fused silica hollow core fiber with drilling holes as gas inlets.

shows the two versions with different lengths that were designed. The tube at the top is the connection to the gas supply. The actual fused silica hollow core fiber[3] is fixed and glued into a V-groove to ensure stability and straightness. To reduce the gas load for the vacuum system as far as possible the only exits into the ambient vacuum should be the fiber capillaries. Sealing, except for the fiber itself of course, is achieved by flanges connected to the V-groove and the glue holding the fiber. To allow gas to enter the capillary from the gas cell the fiber needs to be opened. Initial attempts to use several separate pieces of fiber proved difficult since the position of the core within the fiber is not completely centered due to the manufacturing process. This means that for good alignment, allowing a straight passage of the beam, the rotation of the individual fiber pieces needs to be matched. This was almost impossible to achieve. The solution was to not separate the pieces but cut holes with a high speed diamond drill bit only slightly penetrating into the capillary. The result is shown in section 3.2.1 d). Since only a few *nms* of the cladding are relevant for

[3]LEONI Fiber Optics GmbH

the wave guiding the "cut aways" of the bulk material do not influence this function. To estimate the influence of the cut-outs themselves we can start with a zero order Bessel mode with its zero crossing at the radius of the cladding. Taking the smallest fiber we have with an inner diameter of 100 μm and using a Gaussian mode with the same FWHM as the Bessel mode we get a waist radius of $\omega_0 = 37\ \mu m$. From that we get a Rayleigh range of $z_R = \frac{\pi\omega_0^2}{\lambda} = 2.2\ mm$. Since the cut outs are significantly shorter than 1 mm we can assume the loss by the expansion of the beam over that distance to be negligible.

Since the alignment of the fiber to the beam and focus is crucial for proper in- and through-coupling the cell is mounted on a five-axis (three-axis translational and two-axis rotational) stage.

3.2.2 Tight Focusing Targets

Tight focusing targets are rather simple in design if compared with the just described fiber targets. They consist of a small gas filled tube with a hole drilled into it to allow the laser to pass through. Section 3.2.2 a) shows a tight focusing target made out of steel in use

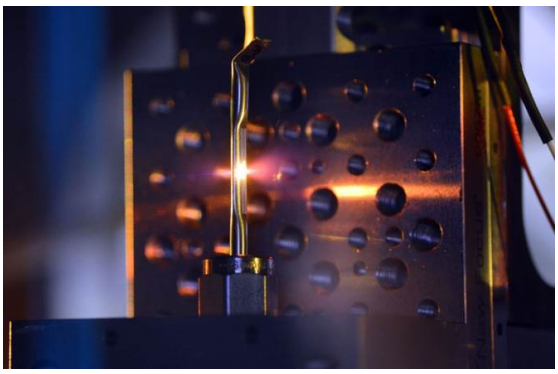

(a) Steel tight focusing HHG target used with a Ti:Sa laser. Clearly visible are the jets of ionized gas and the asymmetry in them due to the after focus position.

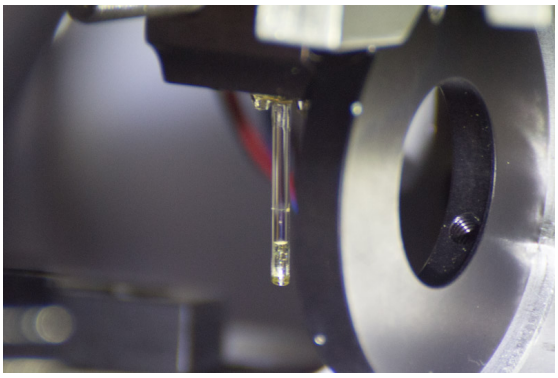

(b) Glass tight focusing target

Figure 3.8: Tight focusing HHG targets in different material versions.

with a Ti:Sa laser. The gas supply here is attached from the bottom. Clearly visible are the jets of ionized gas escaping from the target. The asymmetry in their size is due to the position slightly after focus optimal for HHG (section 1.4.3). Attempts to use these steel targets with the 2 μm laser proved difficult because of the simple fact that the beam is not visible and its adjustment through the target with an attenuated beam was not precise enough. Upon application of the full beam the target would quickly get "burned" opening the hole to an extend that the necessary gas pressures could not be reached anymore. The solution to this problem was the use of glass targets as shown in section 3.2.2 b).

The glass is structurally much more resistant to the 2 μm beam allowing more significant misalignment without damage. A serious disadvantage however is that the glass targets need to be manufactured by a third party company[4] since we do not have the means to drill into glass with the necessary precision.

3.3 Simulations of Pulse Propagation in a Hollow Core Fiber

To get a better understanding of the effects caused by misalignment or beam distortions on the evolution of the pulse and mode I simulated the linear pulse propagation in a hollow core fiber. The simulation uses a Runge-Kutta-4 algorithm to solve the paraxial wave equation. Cylindrical coordinates are used to account for the symmetry of the simulation area (the fiber) but without limiting the possible mode shapes to this symmetry; radius and angle coordinate are both calculated. The transition between capillary and cladding is not treated in a special way. The difference is only the jump in the refractive index which is wavelength dependent, as calculated from the Sellmeier equation. For the simulations shown here the core is assumed to be vacuum while the cladding is SiO_2. To calculate the behavior of a short pulse the simulation is run for multiple frequencies sampling the input spectrum. The beam profiles shown are cuts along the x-z and y-z planes with the propagation direction (z) from top to bottom. The position of the core-cladding border is marked with lines for better visibility. These are added later and are not coming from the simulation. The core in all simulations has a diameter of $d = 140\ \mu m$. The central wavelength is at $\lambda_c = 2\ \mu m$.

The results clearly show the sensitivity of the fiber to alignment. Already small deviations from optimal orientation or position have serious impact on the form of the mode and the pulse although orientation appears to be more important. Also the size of the mode at the point of the incoupling is more important than previously thought. Surprisingly the mode cleaning effect that is always assumed to happen in such fibers can only be witnessed after rather long distances.

Bessel vs. Gaussian mode

Section 3.3 shows a comparison of a perfectly coupled Bessel mode with a comparable Gaussian mode. Perfectly coupled here means zero wavefront curvature (in focus), the first zero of the Bessel function at $r = r_{core}$, and mode centered on the fiber. The Gaussian mode size was chosen that $\int_0^{r_{core}} (J_0(\frac{2.4048 \cdot r}{r_{core}}) - e^{-\frac{r^2}{\sigma^2}})^2 dr$ gets minimal. This is the case for $\sigma \approx 0.72 \cdot r_{core} = 50.4\ \mu m$. a) confirms that a zero order Bessel function is a stable solution for propagation in a HCF, only showing very slight losses without changes in the mode

[4]Workshop of Photonics, Lithuania `https://www.wophotonics.com/`

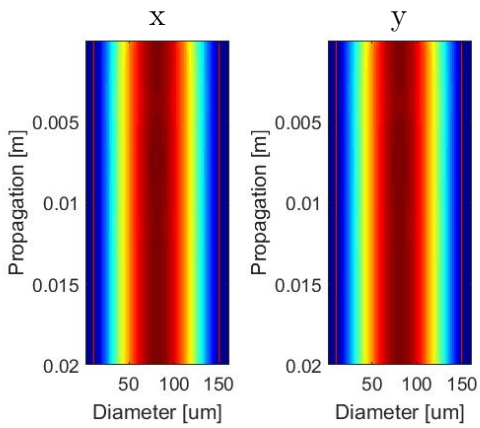

(a) 2 cm propagation of a perfectly coupled zero order Bessel mode

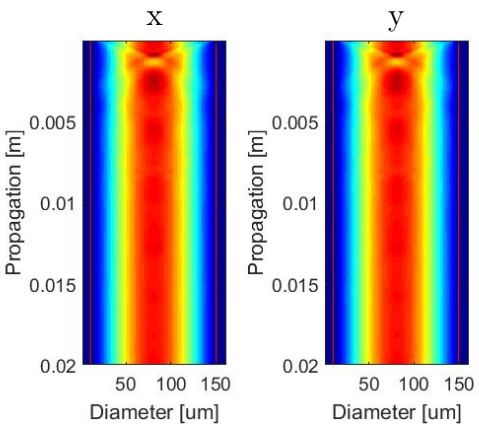

(b) 2 cm propagation of an ideally matched Gaussian mode.

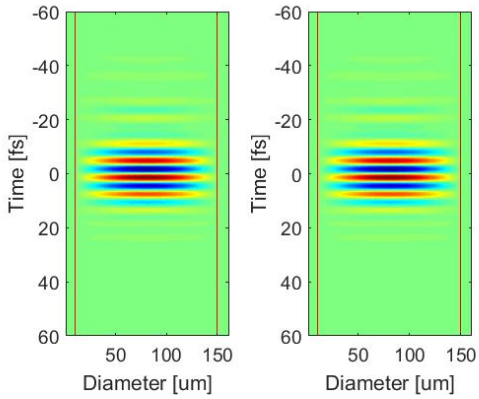

(c) Pulse of the Bessel mode after 2 cm propagation.

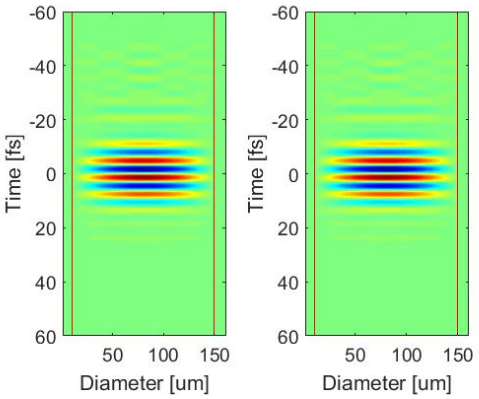

(d) Pulse of the Gaussian mode after 2 cm propagation.

Figure 3.9: Comparison of perfectly coupled Bessel and Gaussian modes. Propagation direction is top to bottom with the fiber edge at $z = 0$. The red lines mark the position of the core-cladding transition. Zero order Bessel modes are a stable solution for propagation in HCFs as a) confirms. b) a coupled in Gaussian mode can lead to close to ideal propagation. Slight incoupling effects are visible though. c-d) The pulses after 2 cm propagation. Only very slight differences are visible.

form. The Gaussian mode in b) results in a similar behavior after a few mm. Some ripples from the not completely ideal incoupling are visible however. Comparing the resulting pulses after the propagation, the differences are negligible. Since Gaussian modes are a usual assumption for the treatment of laser modes in free space all further simulations use these as a starting point.

Incoupling errors

To estimate the sensitivity of the alignment of a fiber I simulated typical incoupling errors. Section 3.3 shows the effects of translational and rotational errors. Although the beam profiles (a, b) for both types look close in the general behavior of an oscillating beam the effect on the pulse shape (c, d) is very different. The rotational error is distorting the spatio-temporal distribution and introducing phase jumps. Also looking at the mode (e,f) it is obvious that no steady state propagation has been reached within this distance making the phase matching scheme we are aiming for impossible.

The effects of a misplacement of the fiber in beam direction by $\pm 2\ mm$ are plotted in section 3.3. Although the pulse is preserved and the propagating mode is not distorted too much, comparison with section 3.3 shows that clear oscillations in the mode size with z-direction are present. These are also visible in the form of wavefront curvature.

Mode size

The importance of matching the size of the beam and the fiber can be seen in section 3.3. I simulated the propagation of a Gaussian beam with 60 % and 140 % of the ideal beam diameter. Both cases lead to increased losses inside the fiber even after the clipping losses of the later case. Also oscillations in the mode are a result of the unmatched sizes. Interestingly with a badly matched mode size a second trailing pulse in a higher order mode is forming. Although also present for the case of a too big mode (d) the effect is much more pronounced for the too small mode (c).

Cleaning astigmatism

The results from an astigmatic beam are shown in section 3.3. The expected effect of mode cleaning and astigmatism removal is there but takes significantly longer than expected. Several cm of fiber are necessary to act as an efficient filter. The input beam was chosen to have an intermediate round mode between foci matching the 50 μm of an ideal Gaussian beam. The fiber entrance was set to this position. The distance between the foci is 4 mm which results in a focus size of 41 μm for the individual foci.

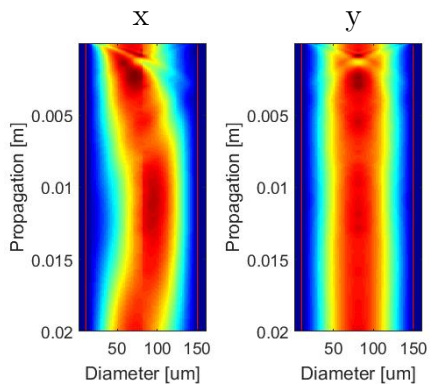

(a) 2 cm propagation of a Gaussian beam of ideal size with a translational incoupling error of 10% of the fiber diameter.

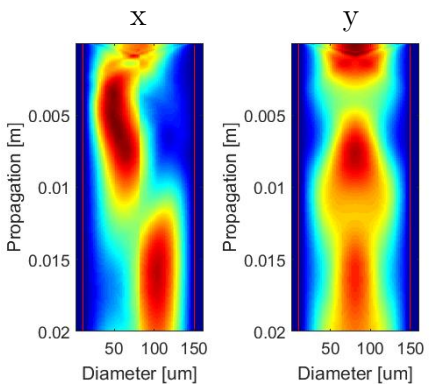

(b) 2 cm propagation of a Gaussian beam of ideal size with a rotational incoupling error of 0.5 *deg*.

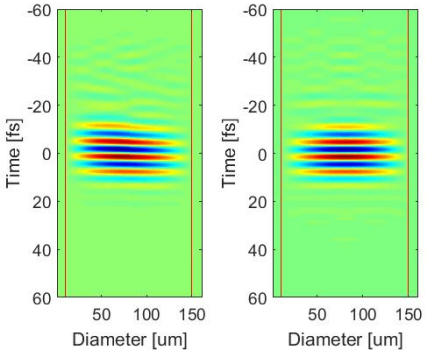

(c) Pulse after 2 cm propagation of a)

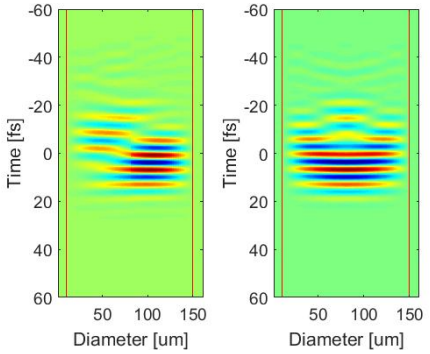

(d) Pulse after 2 cm propagation of b)

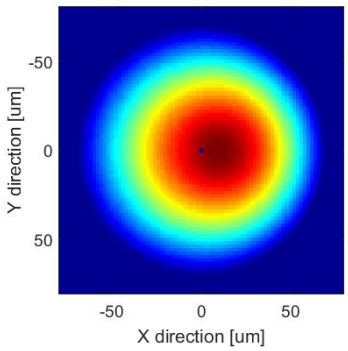

(e) Mode after 2 cm propagation of a)

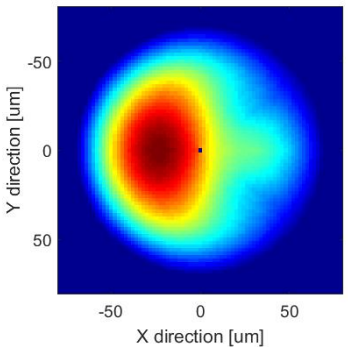

(f) Mode after 2 cm propagation of b)

Figure 3.10: Effects of translational and rotational incoupling errors. a), c), e): While a translation from ideal incoupling leads to additional losses and distortions in the mode, the pulse is mostly unaffected. b), d), f): Rotational incoupling errors also strongly distort the pulse. In both cases the mode after 2 cm is obviously still not in a steady state.

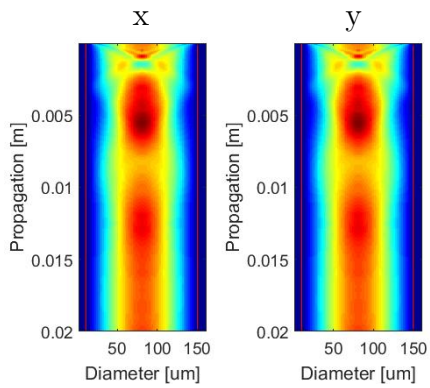

(a) Mode propagation of a Gaussian beam with the focus 2 mm before the fiber entrance.

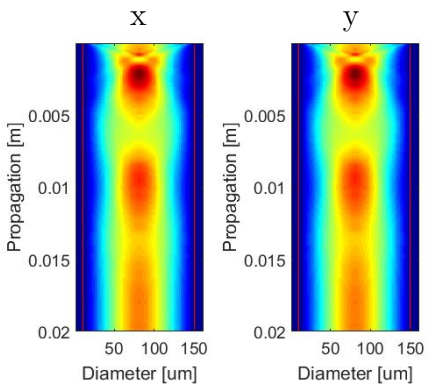

(b) Mode propagation of a Gaussian beam with the focus 2 mm after the fiber entrance.

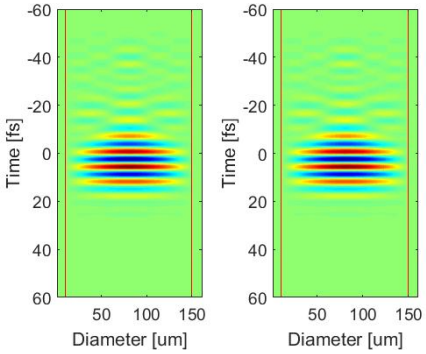

(c) Pulse after 2 cm propagation of a)

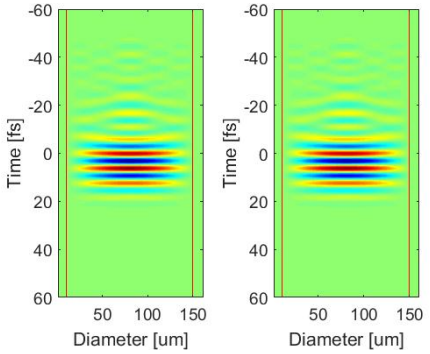

(d) Pulse after 2 cm propagation of b)

Figure 3.11: Effects of a wrong fiber position in z direction. A misplacement of the fiber in the regime of only a few *mm* already causes oscillations in the beam profile. These are also still visible after 2 *cm* in the form of wavefront curvature. The pulse however is preserved and not too much affected.

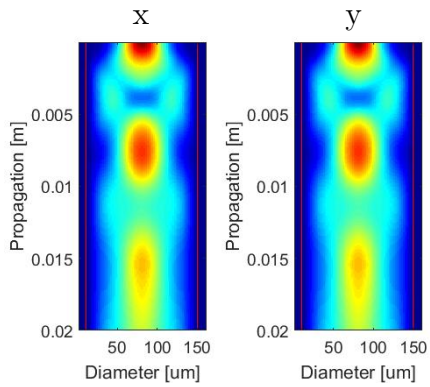

(a) Mode propagation of a Gaussian beam with 60 % of the ideal beam diameter.

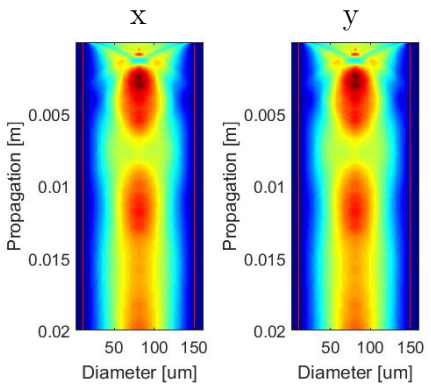

(b) Mode propagation of a Gaussian beam with 140 % of the ideal beam diameter.

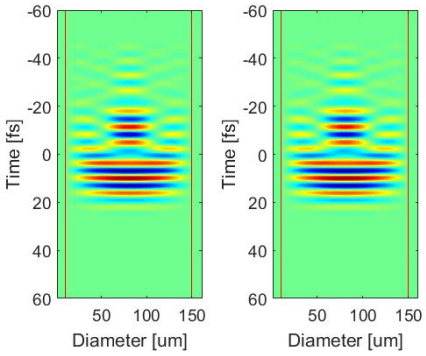

(c) Pulse after 2 cm propagation of a)

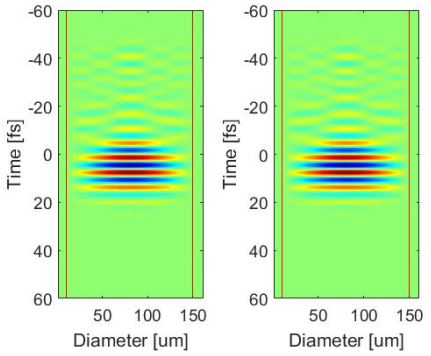

(d) Pulse after 2 cm propagation of b)

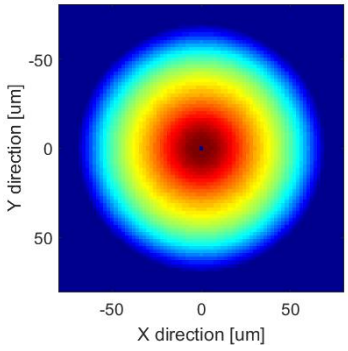

(e) Mode after 2 cm propagation of a)

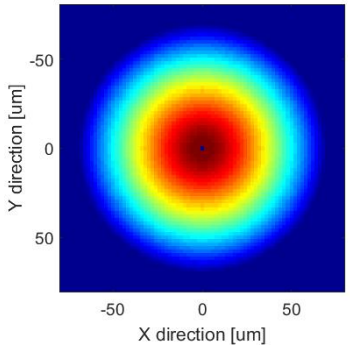

(f) Mode after 2 cm propagation of b)

Figure 3.12: Effects of bad matching of fiber and beam diameter. Propagation of Gaussian beams with initial diameters of 60 % (a) and 140 % (b) of the optimal beam size.

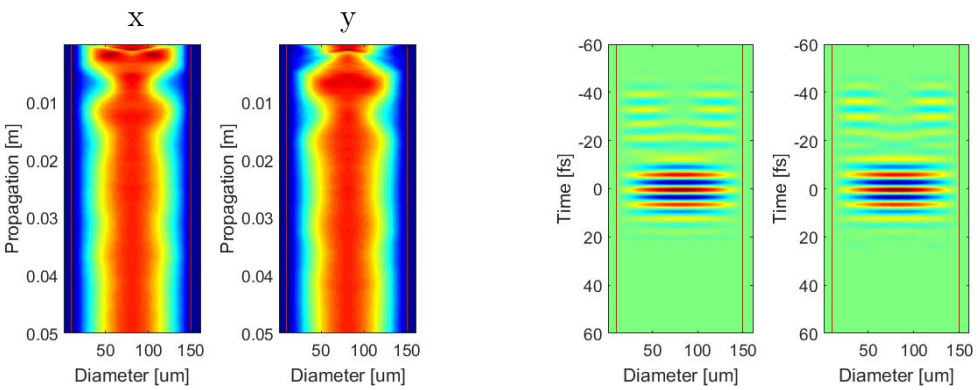

(a) Beam profile.

(b) Pulse after 5 cm

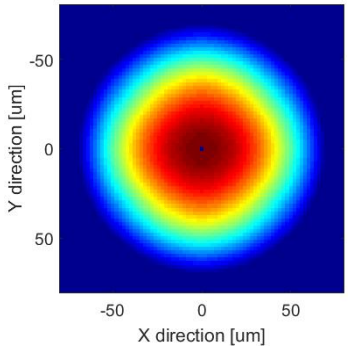

(c) Mode after 5 cm

Figure 3.13: Mode cleaning of an astigmatic beam in a 5 cm long fiber. The distance between the individual foci is 4 mm with the fiber entrance inbetween. The size was chosen that the round mode between foci matches the 50.4 μm of an ideal Gaussian mode.

3.4 Testing of the Waveguide Targets with a Ti:Sa Laser

The goal of this thesis from the start was the generation of high harmonics with a $\lambda = 2\ \mu m$ driver (LWS1). Previously published results from other groups hinted that the waveguide design (section 1.4.3 and section 3.2.1) for targets was a good approach to compensate for the unfavorable wavelength scaling (section 1.4.2) and achieve enough XUV flux for further experiments. We are in the fortunate position to not only have the OPA LWS1 (chapter 2) at our disposal but also a Ti:Sa laser with pulse durations $\tau < 4fs$ and pulse energies $E_{pulse} \approx 0.4\ mJ$ suitable for HHG, FP2. To test the feasibility of the target design, first experiments were conducted using this laser.

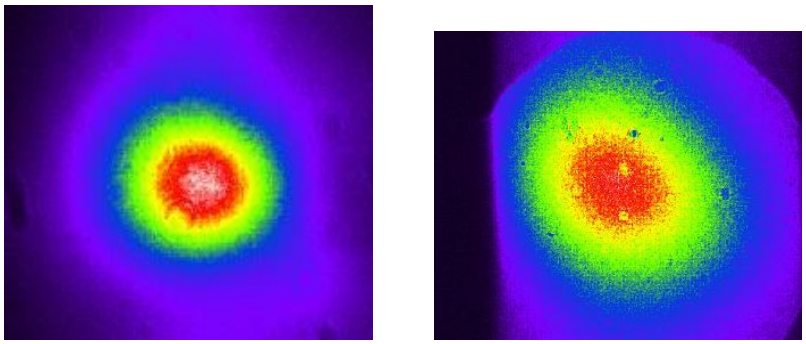

(a) 83 *mbar* argon (b) 993 *mbar* neon

Figure 3.14: XUV modes from a 150 μm capillary with a length of 28 mm in argon and neon.

The XUV modes we could generate with FP2 in a waveguide target are plotted in section 3.4. The capillary had a diameter of $d = 150\ \mu m$, a length of $l = 28\ mm$, and a backing pressures of $p = 83\ mbar$ in argon and 993 $mbar$ in neon respectively. To filter the remaining light from the driving laser two 500 nm thin foils of aluminum for argon and zirconium for neon (section 3.1.3) were placed in front of the camera. Although not perfect, the shape of the generated XUV beam appeared well behaved in shape and stability.

Pressure scans like they are depicted in section 3.4 (a, b) show clear phase matching behavior and similarities to the result of a scan using a conventional tight focusing target (c). Interesting is the shift of the optimum conditions to lower pressures with increasing fiber length for similar photon energy regimes. Discouraging for our plan to switch to a longer wavelength driver however was the fact that the obtained XUV intensities emitted by the fiber targets remained far behind the ones from the conventional one. A new feature unknown from tight focusing targets is a regime of increased high harmonic yield at higher pressures as shown in section 3.4. This was described by Popmintchev et al. [38] and is attributed to spatio-temporal self confinement of the driving laser within the fiber. XUV intensity in this regime was about one order of magnitude higher than at lower pressures but still stayed below what could be achieved with the conventional target. Notable here

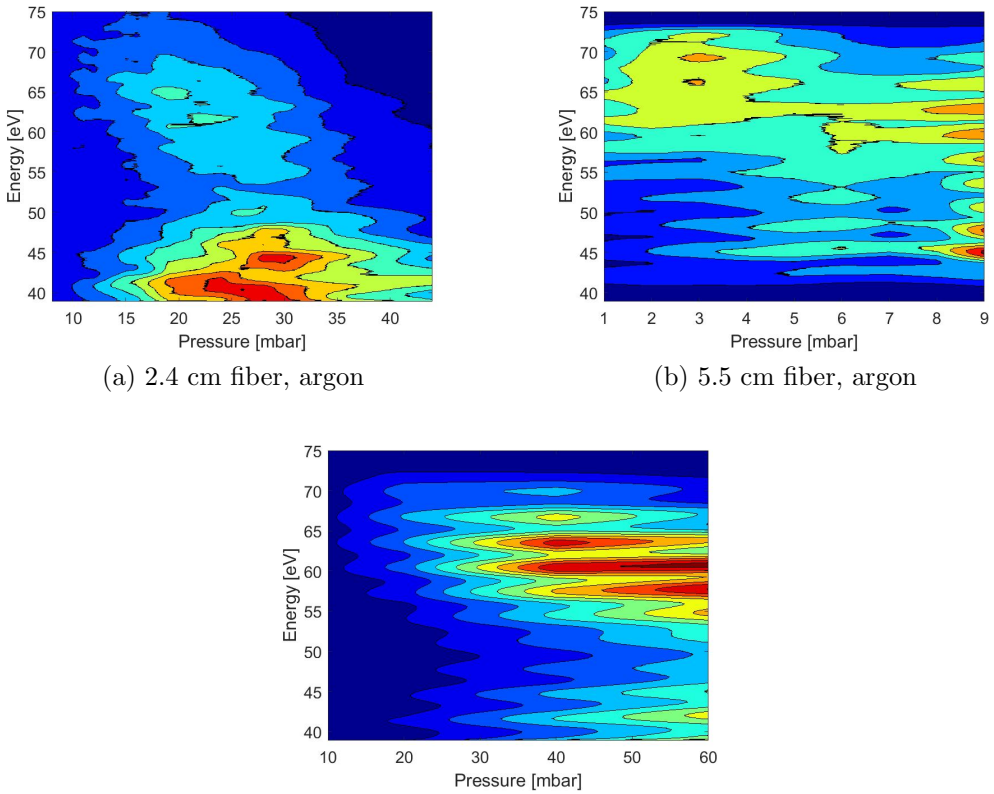

(a) 2.4 cm fiber, argon

(b) 5.5 cm fiber, argon

(c) Conventional target, argon

Figure 3.15: Pressure maps of the XUV spectra generated by a Ti:Sa laser in fiber targets at low pressures (a, b) and a conventional tight focusing target (c) in argon.

is the absence of modulations by different harmonic orders. Regrettably at the time of the experiment no other means for diagnostics were in place and the temporal structure of the XUV in this pressure regime could not be determined.

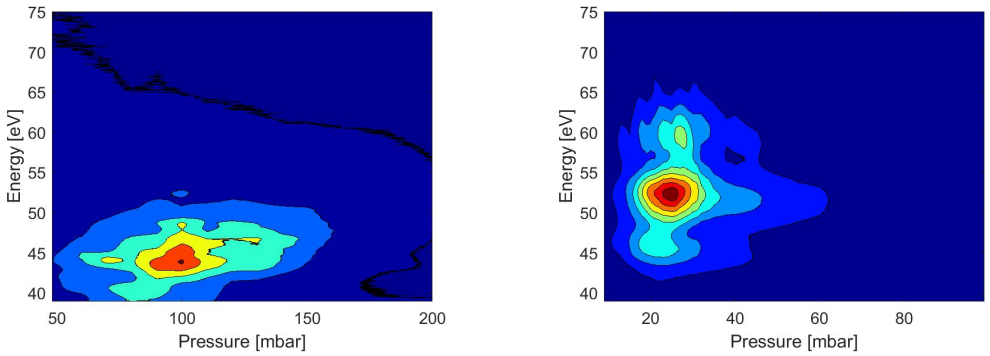

(a) 2.4 cm fiber, argon (b) 5.5 cm fiber, argon

Figure 3.16: Pressure maps of the XUV spectra generated by a Ti:Sa laser in fiber targets at high pressures of argon.

3.5 Focusing a 2 μm Laser for HHG

The use of a laser in the near infrared spectral range opens the door for new optical materials compared with the visible. When working with ultra short pulses in the visible most transmittive optics are unusable because of their destructive influence on the temporal and spatial structure of the beam due to dispersive effects. At $\lambda = 2\ \mu m$ however the class of fluorides becomes interesting because of their close to zero group velocity dispersion as plotted in section 3.5. With $GVD_{BaF_2}(2\ \mu m) = -2.5\ fs^2/mm$ barium fluoride is the

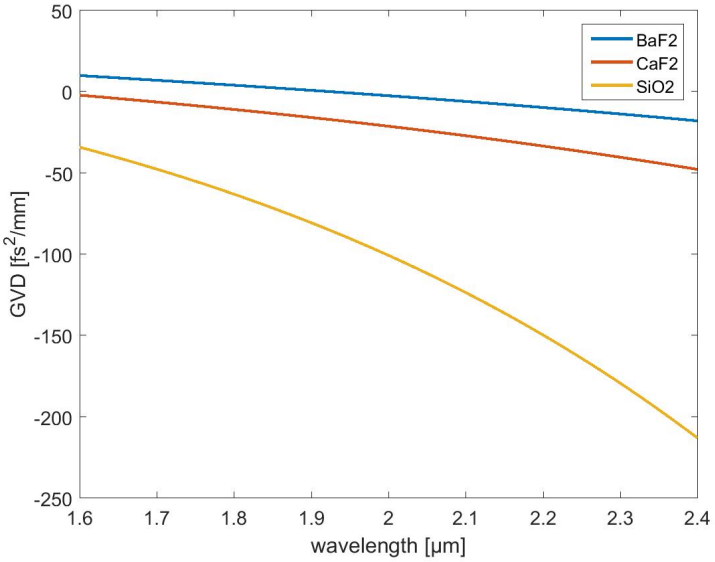

Figure 3.17: Group velocity dispersion of BaF_2, CaF_2, and SiO_2 in the vicinity of 2 μm wavelength.

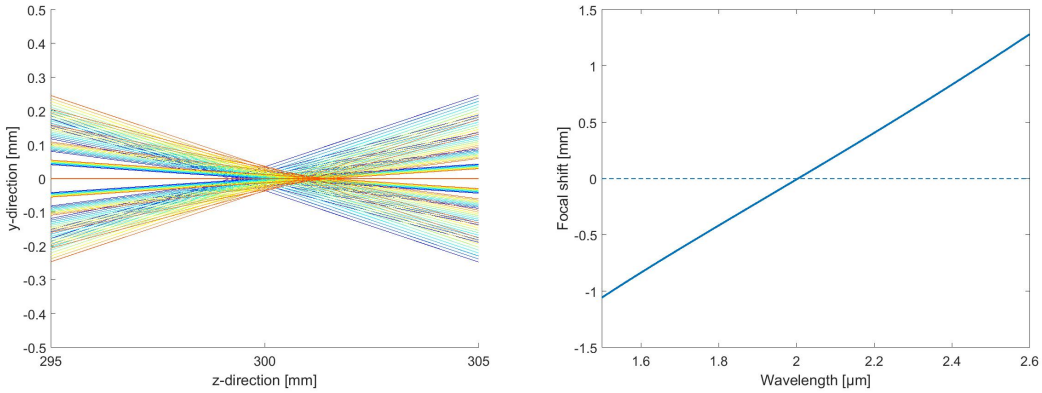

(a) Raytracing image of the spread out focus (b) Shift of the focus position of the individual wavelengths

Figure 3.18: Chromatic spread of the focus of a $f = 30\ cm$ BaF_2 lens for the wavelength range of $\lambda = 1.6 - 2.4\ \mu m$.

most fitting, closely followed by calcium fluoride with $GVD_{CaF_2}(2\ \mu m) = -21.3\ fs^2/mm$; silicon dioxide as a comparison is at $GVD_{SiO_2}(2\ \mu m) = -100.6\ fs^2/mm$. Lenses made from these materials are available commercially. Although close to zero dispersion the effects of chromatic aberrations are not neglectable. Section 3.5 shows the extension of the focus along the propagation direction by this effect. The simple ray tracing image in a) is demonstrating the effect from a spherical, plano convex $f = 30\ cm$, BaF_2 lens on the wavelength range of $\lambda = 1.6 - 2.4\ \mu m$. The shift of the focus position of the individual wavelengths is plotted in b). Due to the decreasing refractive index with wavelength the red is focused up to 3 mm later than the blue. It is to be expected that this, at the very least, reduces the maximum intensity in the focus.
Nonetheless, attempts of high harmonic generation with these lenses were successful. Initially, comparing experiments between lenses and off-axis parabolic mirrors even showed better results for the lenses. This however proved to be due to the more complex and therefore at that time not ideal alignment of parabolas. The final setup as displayed in section 3.1.2, with an additional mirror right after the parabola, decouples the alignment of the parabola from any necessary beam pointing. The then close-to-ideally-focused beam results in ≈ 50 % more XUV flux in comparison with the BaF_2 lenses causing us to switch to mirrors.

Chapter 4

High Harmonic Generation with an Infrared Driver

The tests with the Ti:Sa showed that in principle the waveguide targets worked. Although we could not get any improvement in flux in comparison with conventional targets we proceeded to test them with LWS1. After some initial results shown in section 4.1 it became apparent quickly that the main factor in the improvement of the generated harmonics was not in the high harmonic setup but in the laser. The active beam stabilization we are using (section 3.1.1) enables us to change and optimize many parameters of the OPA while generating harmonics. The key parameters proved to be the delays controlling the temporal overlap of pump and seed in the individual stages as well as the pump powers. Unexpectedly most efficient high harmonic generation was not at maximum pump powers or what we assumed to be ideal temporal pump-seed overlap. A simple power dependence could be excluded by attenuation of the beam. The dominating underlying detrimental effect is the saturation of the OPA in its individual stages and the resulting spatio-temporal distortions caused by it [39]. Since this can be influenced and in some cases avoided by changing the temporal pump-seed overlap and the pump powers we could improve high harmonic generation by modifying these parameters. Although a theoretical system for the classification of spatio-temporal coupling and distortions exists [40] the phenomenon is hard to quantify in an experimental setup. The common measuring techniques for ultra short pulses do not account for spatial dependencies. We found that an imaging spectrometer could be used to at least get a qualitative impression of the effect. This is shown in section 4.2.1.

4.1 Initial Results with the LWS1 in Waveguide Targets

Using a 2.4 *cm* long fiber we were able to generate detectable harmonics with the LWS1 quickly. Pressure scans showed clear phase matching behavior as can be seen in section 4.1. A typical mode and spectrum are plotted in section 4.1. The spectrum and high energy

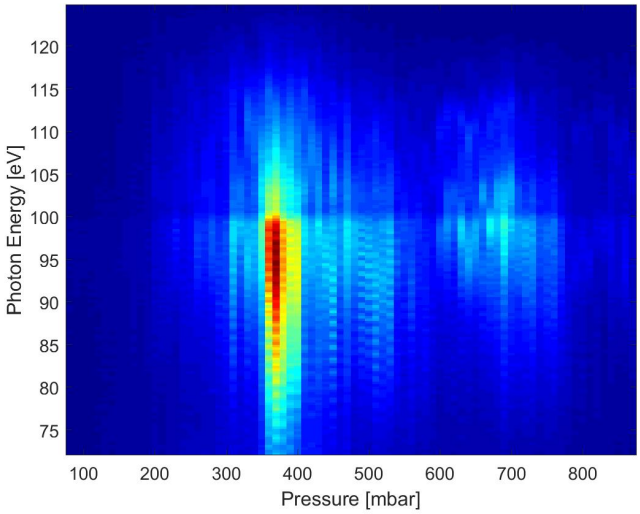

Figure 4.1: Pressure scan of high harmonic generation in argon with a 2.4 *cm* fiber using LWS1. A signature of phase-matching is observed at ≈ 380 *mbar* backing pressure.

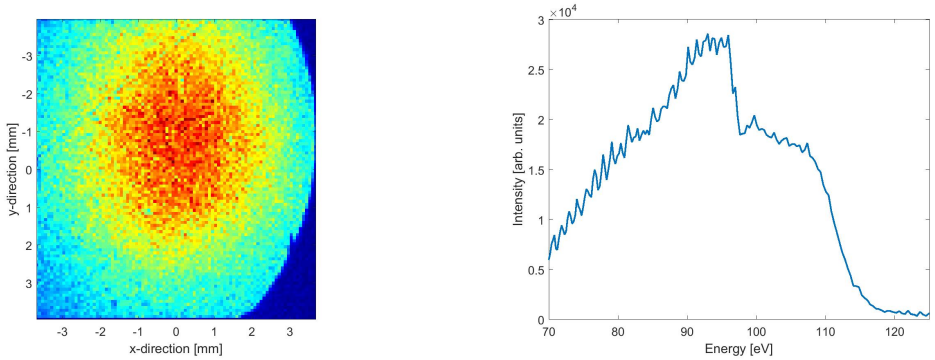

(a) XUV Mode (b) XUV Spectrum

Figure 4.2: Mode and spectrum of high harmonics generated with LWS1 in argon in a fiber with a diameter of $d = 140$ μm and length $l = 2.4$ *cm*.

cut-off (b) look promising. We could generate XUV in argon in the same energy range as with a Ti:Sa in neon. Using the distance from the HHG target and $\omega_0 = \frac{\lambda}{\pi\theta}$ the mode size (section 4.1 a) however suggests for diffraction limited expansion an area of origin of the XUV of under $d = 2\omega_0 < 10\ \mu m$, only a very small fraction of the fiber diameter. An evaluation of the total XUV energy can be obtained from the sum of all counts on the camera I using

$$E_{tot} = \sum_{camera} I \frac{epC \cdot Epe}{f_{rep} \cdot t_{int} \cdot r_{det}} \tag{4.1}$$

with the laser repetition rate f_{rep}, the integration time t_{int} and the manufacturer specified magnitudes 'Electrons per count' epC, 'Energy per electron' Epe and the photon detection rate r_{det}.

This gives an upper limit of $E < 0.2\ pJ$ for the complete XUV pulse train generated per laser shot. The large divergence and low total energy made this unsatisfactory as it is insufficient for the experiments that were planned after establishing HHG. Straightforward optimizations in the HHG setup (fiber diameter and focusing) could not improve this result.

4.2 Saturation in the OPCPA

We found that saturation in the OPA (section 1.3) was not only limiting the maximum possible amplification but that even while the total power of the OPA was still increasing the generated harmonics decreased. One reason for this is the decrease in peak intensity described by Giree et al. [39]. While the total energy in the resulting pulses is still increasing the spatio-temporal compressibility decreases. Furthermore, aside from the described systematic coupling effects, more chaotic behavior is present. Starting from small inhomogeneities in pump or seed saturation at different wavelengths and spatial points sets in after different crystal lengths. The former causes the spectral modulations characteristic for a saturated OPA. The later makes the beam and resulting pulse spatially inhomogeneous. We found that this could be detected using an imaging spectrometer.

4.2.1 Detecting saturation induced beam degradation with an imaging spectrometer

An imaging spectrometer is a spectrometer in which the direction along the entrance slit, perpendicular to the spectral resolution is not integrated but imaged onto a camera. This way it is possible to get a spectrally resolved image of the plane of the slit. In our case we are imaging the focus of our beam. An ideal, homogeneous beam would result in a stretched oval spanning the bandwidth of the laser in the spectral direction and a Gaussian intensity profile in the spatial direction. The camera used is an extended InGaAs camera from Photonic Science[1] with a long wavelength cut-off of $\lambda_{cut} \approx 2.2\ \mu m$ meaning that we can

[1]Now Scintacor `https://scintacor.com/`

not resolve the complete spectral range of our pulse. The most intense and therefore most important spectral region however is well within the detection limit.

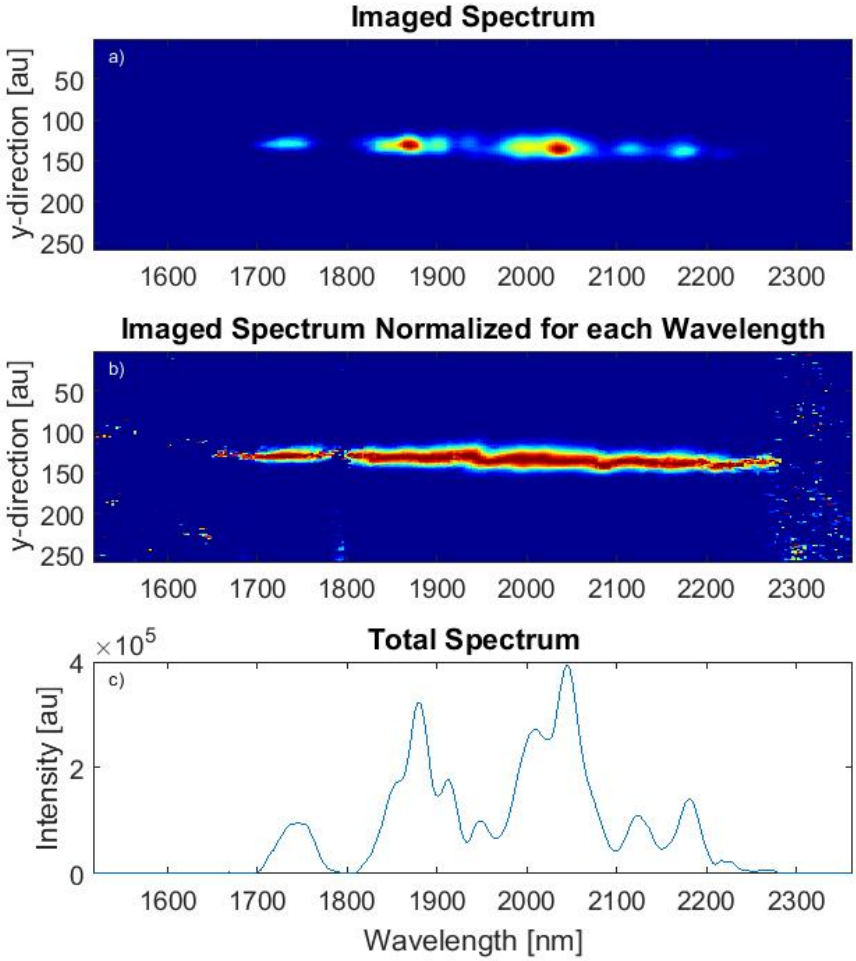

Figure 4.3: Imaged spectra at a seed level of $l = 0.5\%$

To be able to detect the effects of saturation in a repeatable way we found it to be best to not control pump but seed levels. We used the Dazzler before the first amplification stage (section 2.1.3) to control the power of the seed beam. Section 4.2.1 and section 4.2.1 show imaged spectra of the focus of LWS1 after all three stages for input seed levels of 0.5% and 100%. The figures consist of the imaged spectra as recorded by the camera a), the imaged spectra normalized for each wavelength to better see the spatial distribution independent of intensity b), and an integration over the spatial dimension to obtain a conventional spectrum c). Although some distortions are visible already, section 4.2.1, with a seed level of 0.5%, still shows a behavior close to what the ideal would look like. All frequencies have a homogeneous spatial distribution. In section 4.2.1 however a clear

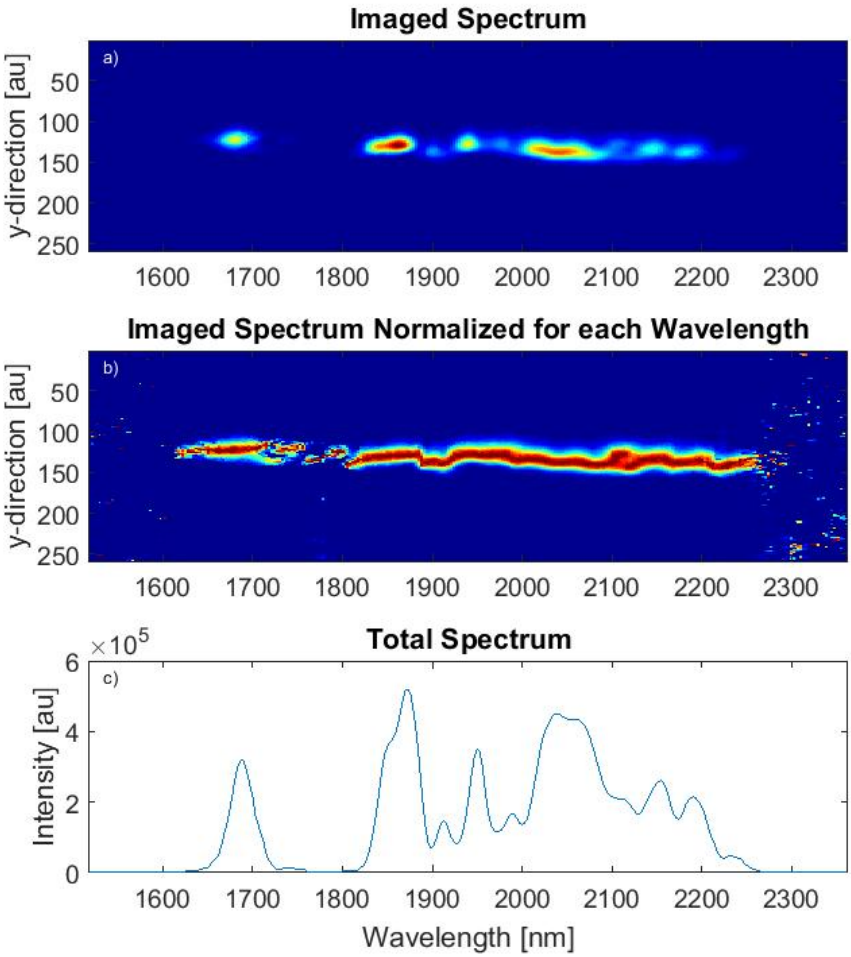

Figure 4.4: Imaged spectra at a seed level of $l = 100\%$

spatial dependence is observable. Spatial shifts between individual spectral regions are on the order of magnitude of one beam diameter. While the more extreme distortions like the ones at $\lambda \approx 1750\ nm$ and $\lambda \approx 2120\ nm$ are located in spectral regions with little power also the high power regions are significantly affected. The spatial distribution of the resulting pulses assuming a flat spectral phase are depicted in section 4.2.1. A clear spatial chirp as well as several more complex distortions are visible. The assumption of a flat and homogeneous spectral phase is most likely incorrect and more distortions from the distribution of the real phase can be expected. Regrettably this is still beyond our means to measure.

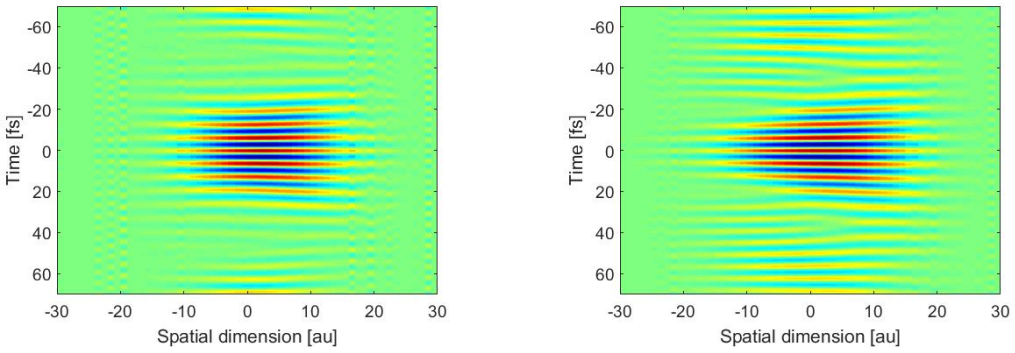

(a) Low seed level and saturation (b) High seed level and saturation

Figure 4.5: Spatial distribution of pulses calculated from the imaged spectra shown in section 4.2.1 and section 4.2.1 assuming a flat spectral phase.

4.2.2 Effects of Saturation in the OPA on High Harmonic Generation

The experimental setup for high harmonic generation starting from the laser, including beam guiding, focusing and ending in the actual high harmonic target is a complex setup with many coupling parameters. This makes it difficult to isolate effects linking the start and end of the described chain. We noticed a strong dependence in the efficiency of HHG on saturation levels in the OPA. Accidentally low seed levels suddenly caused record high harmonic levels and following up on this we could establish that indeed lower saturation levels are beneficial for our experiments despite the lower resulting laser power. To systematically quantify the effect is difficult.

Previous attempts with tight focusing targets (section 3.2.2) using LWS1 resulted in high harmonic levels far below what we could obtain with fiber targets (section 3.2.1). A further attempt with the foreknowledge of the saturation effect however produced similar XUV levels for both target designs. Switching to tight focusing targets simplified the setup by removing the extreme sensitivity to fiber alignment (section 3.3). All data shown here are obtained using a glass tight focusing target (section 3.2.2 b) with an outer diameter of $d = 2.1\ mm$, a core diameter of $d_c = 1.6\ mm$, and a drilled hole diameter of 200 μm.

To study the effect of saturation on HHG, I used the same control mechanism as in the previous section. The level of the OPA is modified by controlling the seed level at the start of the amplification chain with the Dazzler. Variations in beam position and pointing caused by this are caught by the beam stabilization. High harmonics are generated in argon. The resulting XUV spectra are plotted against the seed levels in section 4.2.2 a). Following a steep increase in XUV flux with a clear maximum around 35 % seed level it drops off again. To separate spectral effects from intensity in b) the spectra are

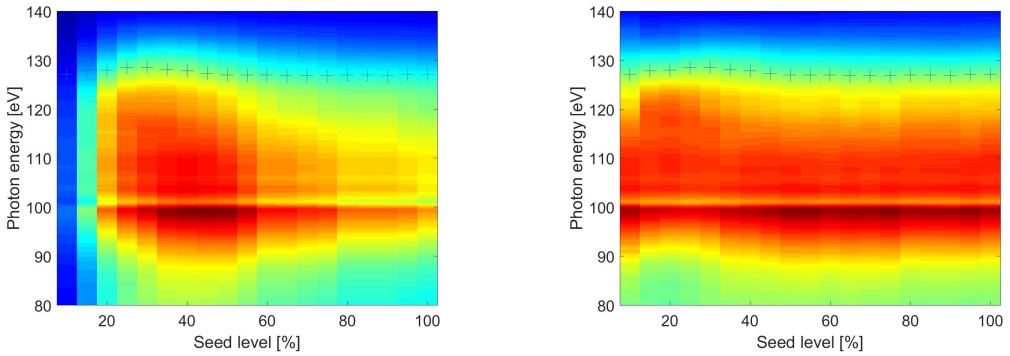

(a) Seed level vs XUV spectrum

(b) Seed level vs XUV spectrum normalized

Figure 4.6: XUV dependence on OPA seed level a). To be able to better observe the high energy cut-off (+) the spectra were normalized to total flux of the respective spectra in b). With increasing seed first a rise in the efficiency of XUV generation and cut-off can be observed. With a further increase the saturation in the OPA limits and even decreases both.

normalized to their respective total counts. An analysis of the high energy cut-off is shown in section 4.2.2. Again a clear maximum can be identified although at slightly lower seed levels than the intensity maximum. The cut-off for this is defined as the position of a threshold in relation to the total counts of the respective spectra. The data points used are marked by the crosses (+) in section 4.2.2.

The imaged spectra for the seed levels of 30 and 40 % during this experiment are plotted in section 4.2.2. A significant spatial jump at $\lambda \approx 1900\ nm$, around the central wavelength is visible between these steps in the vicinity of the cut-off and intensity maxima from section 4.2.2. The imaged spectra of 0.5 and 100 % seed plotted in section 4.2.1 and section 4.2.1 are from the same series.

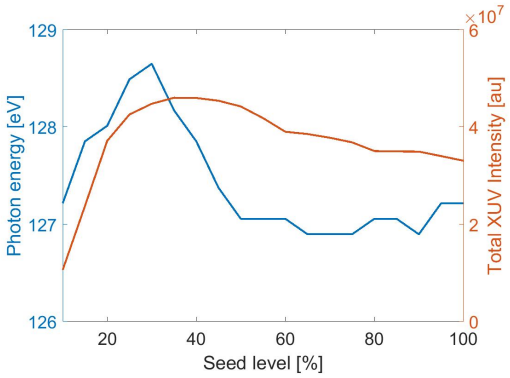

Figure 4.7: Evolution of the high energy cut-off and total intensity from section 4.2.2

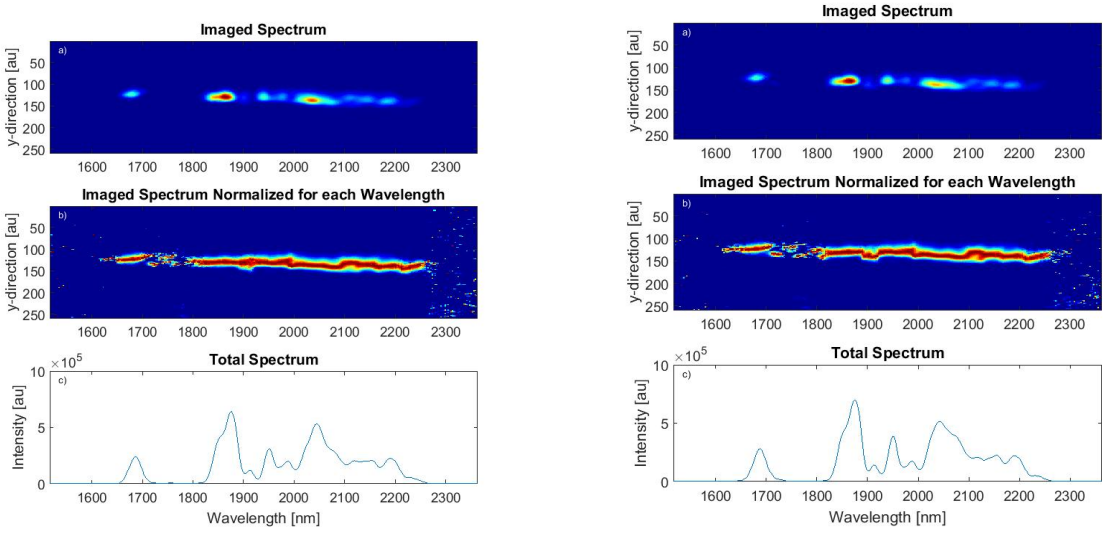

(a) 30 % Seed level

(b) 40 % Seed level

Figure 4.8: Imaged spectra of LWS1 for 30 and 40 % seed level during the series plotted in section 4.2.2 and section 4.2.2.

4.3 Generated XUV

The final setup for high harmonic generation used for attosecond streaking as described in chapter 5 is a tight focusing geometry (section 3.2.2) using a 90° off-axis parabolic mirror with an effective focal length of $f = 8\ in = 20.3\ cm$. After we discovered the previously described OPA saturation effects a comparison of the total XUV flux from tight focusing vs. waveguide targets showed no advantage for the waveguide targets. Due to the significantly lower complexity of the tight focusing targets we decided to proceed with these. Attempts to generate harmonics in neon and extend the high energy cut-off into the water window regrettably were not successful. In one instance we could undoubtedly detect XUV from neon but signal levels were so low we could not even record a spectrum. Since at that time our main goal was to establish enough XUV flux for attosecond streaking we did not undertake further attempts with neon and returned to argon. All further results are from argon.

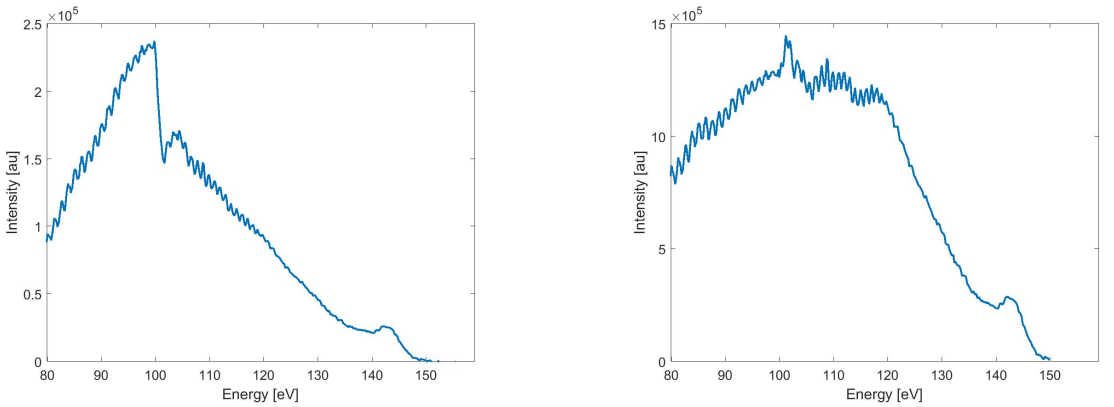

(a) XUV Spectrum

(b) XUV Spectrum corrected for Zr and Si absorption

Figure 4.9: XUV spectrum from a tight focusing target in Ar as used for streaking. The spectrum was recorded with 0.5 μm Zr in the beam. a) depicts the spectrum as recorded, b) with corrections for Si absorption on the camera chip, and the Zr filter in the beam.

A typical spectrum is plotted in section 4.3. a) depicts the spectrum as recorded, b) the spectrum with absorption by the zirconium filters in the beam and the silicon of the camera mathematically removed. The small peak around the Si L-edge near $E = 100\ eV$ in b) is an artifact from that calculation. The XUV was generated in a tight focusing target in 550 $mbar$ Ar. The total energy of the generated pulse train as detected on the camera is $E_{XUV} = 0.3\ pJ$. This is after the silicon and zirconium absorption. Considering the respective absorption spectra this leads to a total XUV energy of $E_{tot} = 14\ pJ$ after generation and still $E_{100\pm5\ eV} = 1.4\ pJ$ reflected by the XUV multilayer mirror used for streaking.

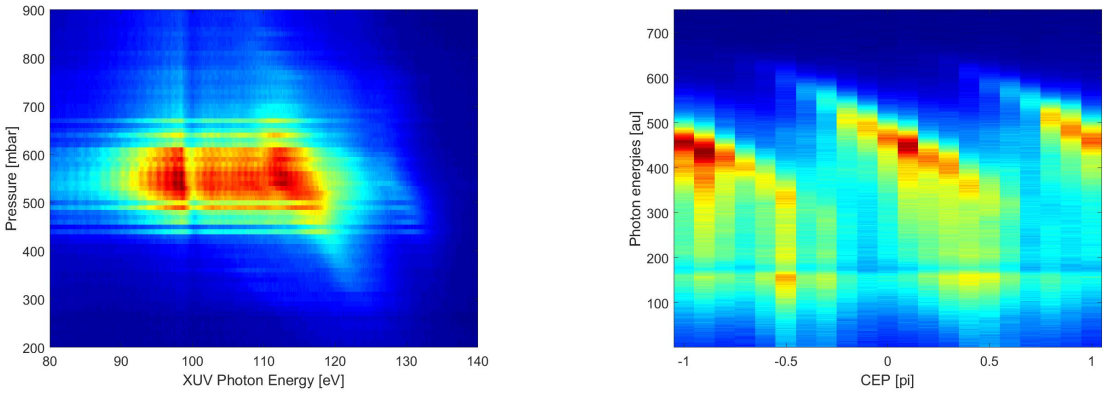

(a) Pressure dependence (b) CEP dependence

Figure 4.10: Dependency of the XUV spectrum on pressure a), and CEP b).

As expected from the phase matching conditions, the XUV intensity is strongly pressure dependent as depicted in section 4.3 a). In b) the strong CEP dependence of our XUV spectrum is plotted, indicating the expected few cycle pulse duration of our laser. The diagonal feature in the high energy regime of a) interestingly can be attributed to a change in CEP within the gas with changing pressure. A rough estimate, neglecting nonlinear effects, shows that the change in the pressure dependent refractive index[41] from $p = 300\ mbar$ to $p = 900\ mbar$ amounts to a change of $\Delta CEP = \pi$ for a distance of $l = 6.5\ mm$ in argon.

Chapter 5

Attosecond streaking

Attosecond streaking was always a long term goal of this thesis and the beamline (section 3.1) was designed from the very start with this in mind. Although techniques like Electro Optic Sampling (EOS) are by now, in this wavelength range, surpassing streaking in dynamic range for the characterization of the driving laser [42], attosecond streaking is still the method to characterize XUV attosecond pulses (section 1.5). Additionally it offers the opportunity to introduce time-resolution to photoemission processes in the involved materials to which other techniques are not sensitive. The goal during this thesis was to establish the technique on a proof of principle basis and this could be achieved.

5.1 Design Considerations

The experimental setup that was used is described and depicted in section 3.1. Due to the short focal length necessary for HHG and the resulting distortions in the IR beam we decided to split off our streaking field before the HHG setup using a SiO_2 beam splitter (section 3.1.2). The ≈ 4 % of the power that was split off is still enough that it needs to be further reduced with an aperture. The loss of ≈ 8 % of the power resulted in no significant decrease in the generation of harmonics. The second reflection from the back of the beam splitter can be separated temporally during streaking. For focusing and overlapping of the IR and XUV beams we decided against a geometry using the toroidal mirror to focus both. Not having to match the divergences and having the IR focus much more insensitive to pointing variations makes the setup significantly easier to handle and adjust to new experimental necessities. Both beams are focused independently, IR with a spherical mirror, XUV with a toroidal mirror, and recombined collinearly with a perforated mirror with the XUV beam passing through the hole (section 3.1.3). The spatial overlap is adjusted by imaging the focal plane onto a Si based camera, using two photon absorption, and the remaining IR passing through the XUV arm. The same system is used to find the temporal overlap by recording an autocorrelation between the arms. It proved extremely helpful to do this in an automated process by scanning the position of the delay stage and evaluating the resulting intensity on the camera. A typical trace is shown in section 5.1. Although

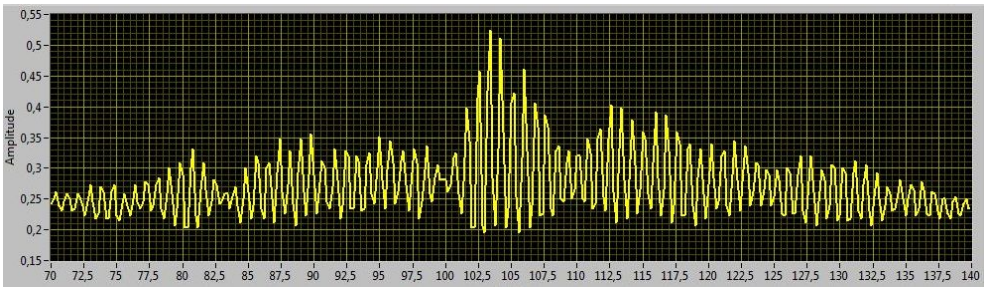

Figure 5.1: Autocorrelation between the IR beam and the remaining IR passing the XUV arm to find the temporal overlap for streaking.

side maxima exist, the overlap is clearly identifiable, making time consuming long range streaking scans to search for temporal overlap unnecessary.

High harmonic generation typically produces a train of attosecond pulses, not just a single one (section 1.4). While theoretically also spectrograms from several pulses can be resolved by the usual reconstruction algorithms, a single isolated pulse makes the interpretation much easier and more robust to errors. Also, for further experiments, precise temporal sampling is only possible with a single pulse. Several techniques to isolate a single pulse have been established, such as polarization gating[43], the attosecond light house[44][45], or spectral gating [30]. We decided to use the later since it is experimentally the most simple one, provided the necessary mirrors are available, and because we have the most experience with it. All data shown in this thesis are taken with a 45° XUV multilayer mirror with a central energy of 100 eV, bandwidth of 10 eV, and maximum reflectivity of 42%. I chose this configuration since it provides the most XUV flux possible while still isolating a single pulse. Although a higher central energy would be desirable all mirrors beyond 100 eV significantly drop in reflectivity due to a necessary change in the used materials. Neon as a medium to generate photoelectrons was chosen because its 2p level with an energy of $E_{2p} = 21.6\ eV$[46] offers a large cross section at 100 eV.

5.2 Photo Electrons

The basis to record streaking spectrograms are electron spectra. We are using a time of flight (TOF) spectrometer with an effective drift tube length of $l = 36\ cm$ in combination with an Agilent[1] counting card with a temporal resolution of $\Delta t = 50\ ps$. This gives us a maximal energy resolution of $\approx 0.1\ eV$ at 80 eV. Since this resolution is not necessary for the experiments performed in this thesis we are using a binning factor of five to reduce the necessary integration times.

[1] now Keysight, `www.keysight.com`

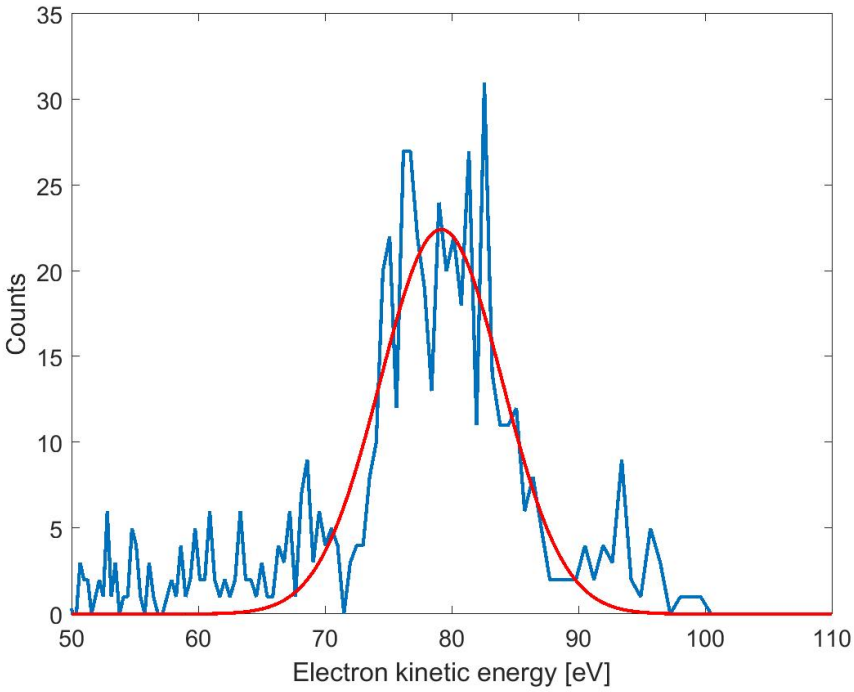

Figure 5.2: Electron spectrum of a 100 eV, 10 eV bandwidth pulse in neon.

A typical electron spectrum without any streaking field is depicted in section 5.2. The fitted Gaussian has a FWHM of 11.3 eV consistent with the bandwidth of the XUV mirror of 10 eV within the precision of the measurement.

5.3 Streaking

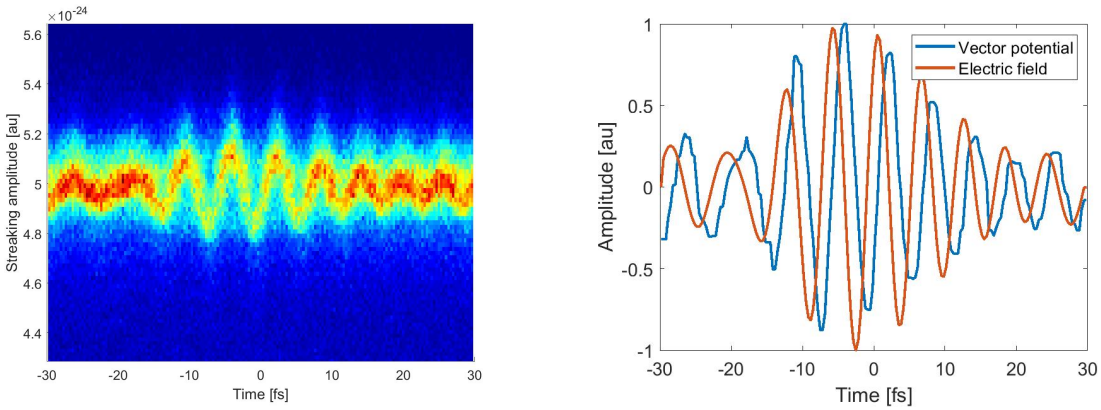

(a) Streaking spectrogram

(b) Resolved vector potential

Figure 5.3: Streaking spectrogram a), and retrieved vector potential and electric field b)

A recorded streaking spectrogram is depicted in section 5.3 a) with its reconstructed vector potential in b). The resolved pulse duration of $FWHM_{IR} = 17\ fs$ is in the regime of two cycles and consistent with pulse characterizations performed via EOS and FROG. The reconstructed attosecond pulse has a duration of $FWHM_{XUV} = 3{\cdot}10^2\ as$ with a neglectable second order chirp of $GDD = -3{\cdot}10^3\ as^2$ and a third order chirp of $TOD = -2.6{\cdot}10^6\ as^3$. To achieve the signal quality necessary for evaluation this spectrogram is a summation of 30 spectrograms recorded in a total time of 105 min. Differences in the individual spectrograms are in the regime of statistical fluctuations indicating a good overall stability of the whole system without significant systematic drifts. For the setup of measurements however already single spectrograms recorded in $\approx 3\ min$ are sufficient to detect the waveform and make any required adjustments.
The evaluation of the spectrogram to retrieve the attosecond pulse is performed with "Attogram" written by Justin Gagnon and based on his "LSGPA" algorithm[47]. The spectrogram is prepared by performing a background substraction. To retrieve the vector potential and electric field, gaussian profiles are fitted to the spectra of the individual time steps and their centers used as the respective streaking amplitude. Before the differentiation to calculate the electric field a Fourier filter excluding wavelength components below $\lambda = 1.5\ \mu m$ is applied.

In section 5.3 no second attosecond pulse is detectable, indicating that the choice of the 100 eV mirror is suitable for the isolation of a single pulse. The importance of a correctly set CEP to isolate a single pulse however is displayed in section 5.3. This spectrogram is recorded with exactly the same configuration except for a different CEP. Clearly visible is the superposition of two spectrograms, almost equal in intensity, shifted by half a laser cycle.

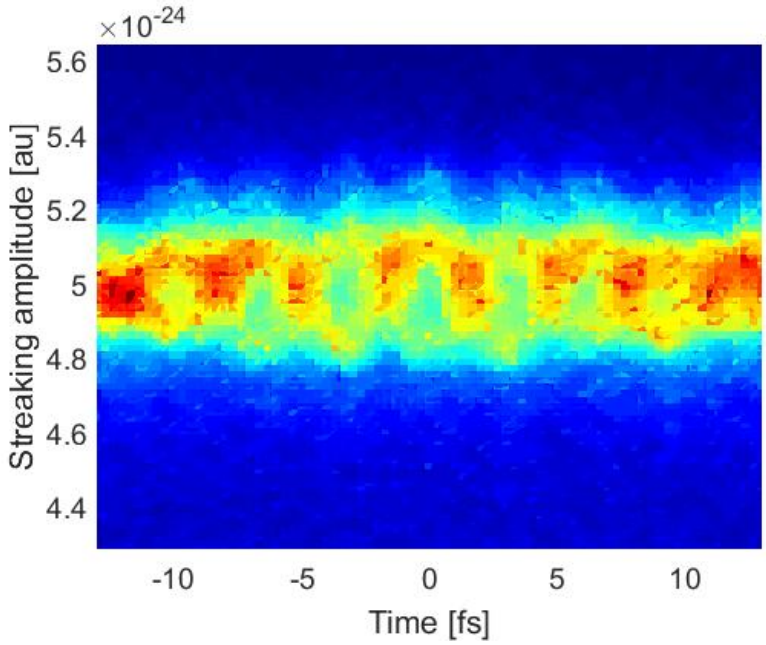

Figure 5.4: Streaking spectrogram with a double XUV pulse

A comparison of the laser spectrum (Ocean Optics NIRQuest) with the Fourier transform of the pulse recorded via streaking is plotted in section 5.3. Within the resolution of the streaking the main distribution fits. Although, due to the short temporal scan range of the streaking, the resolution from it is of course very limited, the bandwidths are similar. The extension further into the red in the streaked spectrum, in comparison with the one recorded from the spectrometer, appears reasonable considering the decreasing sensitivity of the spectrometer in that range.

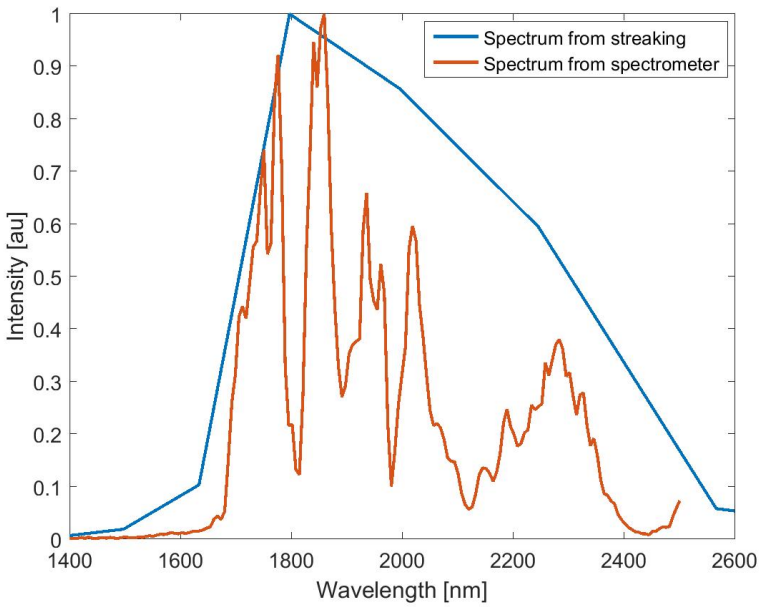

Figure 5.5: Comparison of the laser spectrum (red) with the Fourier transform of the pulse recorded via streaking (blue).

5.4 Delay in Photoemission

One of the early results attosecond metrology could provide was the measurement of the emission delay of photo electrons from different electron levels in neon. The measurements by Schultze et al.[48] showed a time component in a process previously thought to be instantaneous. Although the precision of our measurement was far worse, we were able to repeat the measurement. We were able to record streaking traces simultaneously containing emission lines from the 2s as well as the 2p level of neon. The evaluation of the trace gives an emission delay of $\Delta t = 87 \pm 85\ as$. This of course is no improvement of the measurement but demonstrates the ability to perform similar experiments with the system.

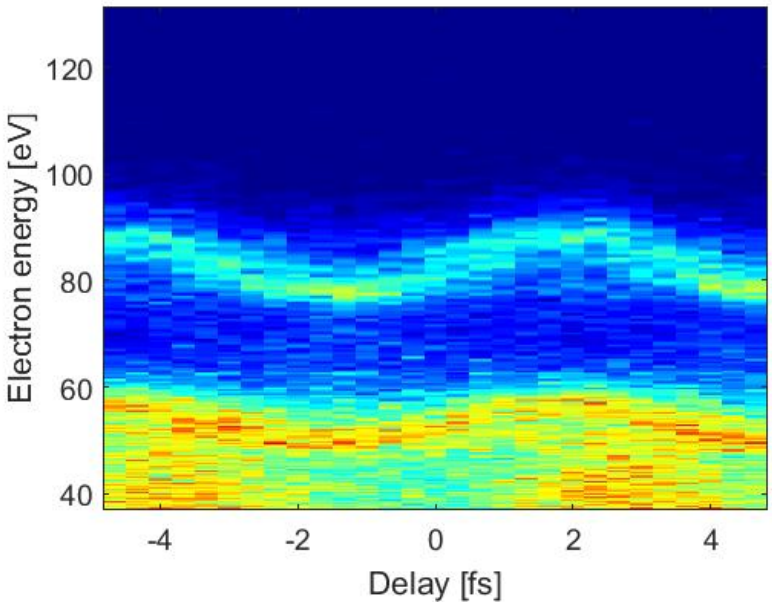

Figure 5.6: Streaked emission lines from the 2s and the 2p level of neon

Chapter 6

Conclusion and Outlook

When I started the work on this thesis we had several long term goals in mind. The framework that high harmonic generation should be transferred into the world of near infrared lasers was clear but a lot of details were left open. We expected to significantly increase the high energy cut off and hoped to be able to extend it into the water window, the regime of photon energies between the carbon K-edge at 282 eV and the oxygen K-edge at 533 eV, where water is transparent but carbon absorbing. This regime would be specifically interesting for the observation of organic samples [49]. We designed a new kind of gas target from results previously published by other groups, before our laser was really operational and were confident this would work. In the end some things we thought easy were the ones that proved difficult or impossible and some that we expected to be hard simply worked.

We did not get the cut off into the water window. A weak signal could be detected, but the flux was simply insufficient by far. We could not even measure a spectrum to validate what we are seeing. The predesigned target proved to be no improvement but only to add complications.

After setting the goal of high cut off energies aside, and retiring some technical ideas, we did generate sufficient XUV flux to be usable for further experiments. We generated isolated attosecond pulses in the same energy regime as established techniques do, but with the important difference that we now have a synchronized, near infrared pulse with almost triple the wavelength available for experiments. With that, lower band gap materials like semiconductors become accessible for investigation and the resolution for effects depending on the subcycle evolution of the driving field increases. We were able to implement attosecond streaking and could characterize our driving pulse. We performed a proof of principle experiment with it, again utilizing the synchronized near infrared pulse, showing the suitability of the system for future experiments. Although these successes are not everything we were aiming for, they are a big step forward in our ability to investigate nature on the attosecond timescale. Furthermore, we learned some important lessons on the way there.

We learned that the challenges we experienced were mostly not originating from our HHG setup but coming from an effect in the OPA that was previously not given sufficient attention. The effect of saturation in optical parametric amplification as such is well

known. Its impact on pulse and focus quality, specifically in broadband OPAs, is often not considered thoroughly enough and is often seen as purely beneficial, as it leads to a reduction in energy fluctuations. The key to the results in this thesis was the finding that saturation needs to be avoided under any circumstances if the application is sensitive to the spatiotemporal form of the light. Even if the resulting pulse energy is only half of what would be possible otherwise, an unsaturated OPA is better suited for high harmonic generation. We found methods to detect and prevent saturation and could improve our system sufficiently to reach the results described in this thesis.

We built a working setup for the generation of high harmonic radiation and subsequent attosecond streaking with a near infrared driver. Since the limiting challenges we encountered were mostly with the laser used, this HHG setup is ready and waiting for future use with new or improved lasers currently under development. The insights gained during the work on this thesis are already used to improve the OPA, LWS1. New lasers currently under development in our group are also promising candidates to utilize the devised high harmonic setup. Together with these new sources the work performed for this thesis will hopefully continue to extend our abilities to investigate nature on the ultrafast timescale even further.

Appendix A

List of Publications

- **C. Jakubeit**, M. Weidman, O. Razskazovskaya, E. Ridente, N. Karpowicz, F. Krausz
  "Effects of saturation on the spatio-spectral distribution of an OPA and its significance for HHG", in preparation
  The author developed the infrastructure, devised and performed the measurements, evaluated the data, and prepared the manuscript together with NK

- A. Sommer, E. Bothschafter, S. A. Sato, **C. Jakubeit**, T. Latka, O. Razskazovskaya, H. Fattahi, M. Jobst, W. Schweinberger, V. Shirvanyan, V. Yakovlev, R. Kienberger, K. Yabana, N. Karpowicz, M. Schultze, F. Krausz
  "Attosecond nonlinear polarization and light-matter energy transfer in solids", Nature 534, 86 (2016)
  The author devised and built crucial parts of the measurement hard- and software, and assisted in the execution of the measurements.

- Keiber, S., Paasch-Colberg, T., Schwarz, A., Razskazovskaya, O., Fedulova, E., Saglam, Ö., **Jakubeit, C.**, Sederberg, S., Dombi, P., Karpowicz, N., Krausz, F.,
  "Investigation of laser-induced currents in large-band-gap dielectrics" Ultrafast Phenomena XIX, Springer Proceedings in Physics. Springer International Publishing, 237-240 (2015)
  The author supported the construction of the experimental setup and assisted in the operation of the used laser.

- J. Schötz, B. Förg, W. Schweinberger, I. Liontos, H.A. Masood, A. Kamal, **C. Jakubeit**, N. G. Kling, T. Paasch-Colberg, M. Högner, M. Alharbi, F. Krausz, M.F. Kling, and A.M. Azzeer
  "Ionization induced transient phase-matching in isolated attosecond pulse generation with few-cycle pulses in argon", Nature Communications, submitted
  The author assisted in the construction of the used experimental setup by establishing HHG in the then new beamline.

- T. Latka, V. Shirvanyan, M. Ossiander, O. Razskazovskaya, A. Guggenmos, M. Jobst, M. Fiess, S. Holzner, A. Sommer, M. Schultze, **C. Jakubeit**, J. Riemensberger, B.

Bernhardt, W. Helml, F. Gatti, B. Lasorne, D. Lauvergnat, P. Decleva, G. J. Halasz, A. Vibok, R. Kienberger
"Few-Femtosecond Wave Packet Revivals in Ozone", Nature Physics, submitted.
The author contributed to the measurement setup and assisted in the execution of the measurements during his masters thesis

- A. Guggenmos, M. Jobst, M. Ossiander, S. Radünz, J. Riemensberger, M. Schäffer, A. Akil, **C. Jakubeit**, P. Böhm, S. Noever, B. Nickel, R. Kienberger, U. Kleineberg
"Chromium/scandium multilayer mirrors for isolated attosecond pulses at 145 eV", Optics Letters 40, 2846 (2015)
The author assisted the execution of the measurements during his masters thesis

Appendix B

Data Preservation

The archived data is stored on `//AFS/ipp-garching.mpg.de/mpq/lap/publication_archive` of the AFS system of the Max-Planck-Institute of Quantum Optics. For each figure exists a seperate folder with the relevant original data and evaluating scripts.

B.1 Figures

- Section 1.1.2: Schematic plot (.jpg) and generating script (.m)
- Section 1.1.2: Schematic plot (.jpg) and generating script (.m)
- Section 1.3: Sketch (.pdf, .ai)
- Section 1.3: Schematic plot (.jpg) and 2 x generating script (.m)
- Section 1.4: Sketch (.pdf, .ai)
- Section 1.4.1: Sketch (.pdf, .ai)
- Section 1.4.1: Plot (.jpg), original data, and plotting script (.m)
- Section 1.4.3: 2 x plots (.jpg), generating script (.m)
- Section 1.4.3: Sketch (.pdf, .ai)
- Section 1.4.3: Sketch (.pdf, .ai)
- Section 1.5: Sketch (.pdf, .ai)
- Section 1.5: Simulation and plotting scripts (.m), plots (.jpg), simulation results (.mat)
- Section 1.5: Simulation and plotting scripts (.m), plots (.jpg), simulation results (.mat)

- Section 2.1: Sketch (.pdf, .ai)
- Section 2.1.1: Plot (.jpg), plotting script (.m), original data (.txt)
- Section 2.1.3: Sketch (.pdf, .ai)
- Section 2.1.3.1: 2 x plots (.jpg), plotting script (.m), 3 x original data (.txt)
- Section 2.2: Plot (.jpg), original data (.txt), calculation and plot (.m)
- Section 3.1: Sketch (.pdf, .ai)
- Section 3.1.1: Sketch (.pdf, .ai)
- Section 3.1.2: Sketch (.pdf, .ai)
- Section 3.1.3: Sketch (.pdf, .ai)
- Section 3.1.3: Plot (.jpg), plotting script (.m), 4x data from cxro.org
- Section 3.1.4: Sketch (.pdf, .ai)
- Section 3.2.1: Fotos (.jpg)
- Section 3.2.2: Fotos (.jpg)
- Section 3.3 - section 3.3: plots (.jpg) All simulation results with their generating matlab code are in individual folders. The script for evaluation and plotting is in the top level folder. Matlab library functions are in the respective folder.
- Section 3.4: 2 x image (.jpg)
- Section 3.4 & Section 3.4: 5 x plots (.jpg), plotting script (.m), original data in 5 subfolders
- Section 3.5: Plot (.jpg), generating script and supporting script (.m)
- Section 3.5: 2 x Plots (.jpg), 2 x plotting scripts (.m), data from Zemax (.txt)
- Section 4.1: Plot (.jpg), plotting script (.m), original data in folder
- Section 4.1: 2 x plots (.jpg), 2 x plotting scripts (.m), supporting script (.m), 2 x original data
- Section 4.2.1-Section 4.2.1 & Section 4.2.2: 6 x plots (.jpg), 2 x plotting scripts (.m), calibration file (.mat), 2 x original data (folder)
- Section 4.2.2 & Section 4.2.2: 3 x plot (.jpg), original data calibration spectrum, plot calibration spectrum (.jpg), energy scale from calibration spectrum (.mat), plotting script (.m), original data (folder)

- Section 4.2.2: at Section 4.2.1
- Section 4.3: 2 x plot (.jpg), plotting script (.m), original data (folder), 2 x data from CXRO (.txt)
- Section 4.3: 2 x plot (.jpg), 2 x plotting script (.m), 2 x original data (folder)
- Section 5.1: Screenshot (.jpg)
- Section 5.2: Plot (.jpg), plotting and supporting script (.m), original data
- Section 5.3 & Section 5.3: 3 x plot (.jpg), 2 x evaluation and plotting scripts (.m), readme (.txt), original data (folder)
- Section 5.3: Plot (.jpg), plotting script and supporting script (.m), original data (.txt), data from section 5.3 (.mat), readme (.txt)
- Section 5.4: Plot (.jpg), evaluation and plotting scripts (.m), readme (.txt), original data (folder)

B.2 Data evaluation

- Section 4.3: Script to calculate the total XUV energy from a recorded beam profile (.m), original data
- Section 5.3: The program "Attogram" (folder), script to prepare the data for attogram (.m). The data is in the folder for section 5.3.
- Section 5.4: Script to sum streaking spectrograms (.m), script to fit emission delay and supporting scripts by Nick Karpowicz (.m), original data

Bibliography

[1] C.C.W Taylor. *The Atomists: Leucippus and Democritus: Fragments (Phoenix Presocractic Series)*. University of Toronto Press, Scholarly Publishing Division, 2010.

[2] P. Ball. *The Elements: A Very Short Introduction*. OUP Oxford, 2004.

[3] G. Aad, et al. Observation of a new particle in the search for the Standard Model Higgs boson with the ATLAS detector at the LHC. *Physics Letters, Section B: Nuclear, Elementary Particle and High-Energy Physics*, 716(1):1–29, 2012.

[4] B. P. Abbott, et al. Observation of Gravitational Waves from a Binary Black Hole Merger. *Physical Review Letters*, 116(6):061102, feb 2016.

[5] Pangratios Papacosta. Muybridge, the Galloping Horse and revealed Errors in Art. *International Journal of Art and Art History*, 6(1):15–26, 2018.

[6] PB Corkum. Plasma perspective on strong field multiphoton ionization. *Physical Review Letters*, 71(13):1994–1997, 1993.

[7] Jie Li, Xiaoming Ren, Yanchun Yin, Kun Zhao, Andrew Chew, Yan Cheng, Eric Cunningham, Yang Wang, Shuyuan Hu, Yi Wu, Michael Chini, and Zenghu Chang. 53-attosecond X-ray pulses reach the carbon K-edge. *Nature Communications*, 8(1):1–5, 2017.

[8] Thomas Gaumnitz, Arohi Jain, Yoann Pertot, Martin Huppert, Inga Jordan, Fernando Ardana-Lamas, and Hans Jakob Wörner. Streaking of 43-attosecond soft-X-ray pulses generated by a passively CEP-stable mid-infrared driver. *Optics Express*, 25(22):27506, 2017.

[9] Bahaa E.A. Saleh and Malivin Carl Teich. *Fundamentals of photonics*. Wiley, 2007.

[10] T. H. Maiman. Stimulated optical radiation in Ruby. *Nature*, 187(4736):493–494, 1960.

[11] F. J. McClung and R. W. Hellwarth. Giant optical pulsations from ruby. *Journal of Applied Physics*, 33(3):828–829, 1962.

[12] L. E. Hargrove, R. L. Fork, and M. A. Pollack. Locking of hene laser modes induced by synchronous intracavity modulation. *Applied Physics Letters*, 5(1):4–5, 1964.

[13] R. L. Fork, B. I. Greene, and C. V. Shank. Generation of optical pulses shorter than 0.1 psec by colliding pulse mode locking. *Applied Physics Letters*, 38(9):671–672, may 1981.

[14] De Spence, Pn Kean, and W Sibbett. 60-fsec pulse generation from a self-mode-locked Ti: sapphire laser. *Optics Letters*, 16(1):42–44, 1991.

[15] A. McPherson, G. Gibson, H. Jara, U. Johann, T. S. Luk, I. A. McIntyre, K. Boyer, and C. K. Rhodes. Studies of multiphoton production of vacuum-ultraviolet radiation in the rare gases. *Journal of the Optical Society of America B*, 4(4):595, 1987.

[16] M Drescher, M Hentschel, R Kienberger, G Tempea, C Spielmann, G a Reider, P B Corkum, and F Krausz. X-ray pulses approaching the attosecond frontier. *Science (New York, N.Y.)*, 291(5510):1923–7, mar 2001.

[17] N. H. Burnett, H. A. Baldis, M. C. Richardson, and G. D. Enright. Harmonic generation in CO2 laser target interaction. *Applied Physics Letters*, 31(3):172, 1977.

[18] M Lewenstein, P Balcou, and MY Ivanov. Theory of high-harmonic generation by low-frequency laser fields. *Physical Review A*, 49(3), 1994.

[19] M Fieß. *Advancing attosecond metrology*. PhD thesis, Ludwig-Maximilians-Universität München, 2010.

[20] Jeffrey L. Krause, Kenneth J. Schafer, and Kenneth C. Kulander. High-order harmonic generation from atoms and ions in the high intensity regime. *Physical Review Letters*, 68(24):3535–3538, 1992.

[21] S M Teichmann, F Silva, S L Cousin, M Hemmer, and J Biegert. 0.5-keV Soft X-ray attosecond continua. *Nature Communications*, 7(1):11493, dec 2016.

[22] Seth L. Cousin, Nicola Di Palo, Bárbara Buades, Stephan M. Teichmann, M. Reduzzi, M. Devetta, A. Kheifets, G. Sansone, and Jens Biegert. Attosecond streaking in the water window: A new regime of attosecond pulse characterization. *Physical Review X*, 7(4):1–14, 2017.

[23] J. Tate, T. Auguste, H. Muller, P. Salières, P. Agostini, and L. DiMauro. Scaling of Wave-Packet Dynamics in an Intense Midinfrared Field. *Physical Review Letters*, 98(1):013901, jan 2007.

[24] A. D. Shiner, C. Trallero-Herrero, N. Kajumba, H. C. Bandulet, D. Comtois, F. Légaré, M. Giguère, J. C. Kieffer, P. B. Corkum, and D. M. Villeneuve. Wavelength scaling of high harmonic generation efficiency. *Physical Review Letters*, 103(7):1–4, 2009.

[25] Tenio Popmintchev, Ming-Chang Chen, Alon Bahabad, Michael Gerrity, Pavel Sidorenko, Oren Cohen, Ivan P Christov, Margaret M Murnane, and Henry C Kapteyn. Phase matching of high harmonic generation in the soft and hard X-ray regions of the spectrum. *Proceedings of the National Academy of Sciences of the United States of America*, 106(26):10516–21, jun 2009.

[26] Philippe Balcou, Pascal Sali'eres, Anne L'Huillier, and Maciej Lewenstein. Generalized phase-matching conditions for high harmonics: The role of field-gradient forces. *Physical Review A*, 55(4):3204–3210, 1997.

[27] Tenio Popmintchev, Ming-Chang Chen, Paul Arpin, Margaret M. Murnane, and Henry C. Kapteyn. The attosecond nonlinear optics of bright coherent X-ray generation. *Nature Photonics*, 4(12):822–832, dec 2010.

[28] D. E. Rivas, A. Borot, D. E. Cardenas, G. Marcus, X. Gu, D. Herrmann, J. Xu, J. Tan, D. Kormin, G. Ma, W. Dallari, G. D. Tsakiris, I. B. Földes, S. W. Chou, M. Weidman, B. Bergues, T. Wittmann, H. Schröder, P. Tzallas, D. Charalambidis, O. Razskazovskaya, V. Pervak, F. Krausz, and L. Veisz. Next Generation Driver for Attosecond and Laser-plasma Physics. *Scientific Reports*, 7(1):1–8, 2017.

[29] E Goulielmakis and M Uiberacker. Direct measurement of light waves. *Science*, 305(August):1267–1269, 2004.

[30] Reinhard Kienberger, Eleftherios Goulielmakis, and M. Uiberacker. Atomic transient recorder. *Nature*, 427:817–821, 2004.

[31] J. Gagnon and V. S. Yakovlev. The direct evaluation of attosecond chirp from a streaking measurement. *Applied Physics B: Lasers and Optics*, 103(2):303–309, 2011.

[32] V. S. Yakovlev, J. Gagnon, N. Karpowicz, and F. Krausz. Attosecond streaking enables the measurement of quantum phase. *Physical Review Letters*, 105(7):3–6, 2010.

[33] Alexander Hermann Schwarz. *Few-cycle phase-stable infrared OPCPA*. PhD thesis, Ludwig-Maximilians-Universität München, 2014.

[34] Thomas Metzger, Alexander Schwarz, Catherine Yuriko Teisset, Dirk Sutter, Alexander Killi, Reinhard Kienberger, and Ferenc Krausz. High-repetition-rate picosecond pump laser based on a Yb:YAG disk amplifier for optical parametric amplification. *Optics Letters*, 34(14):2123, 2009.

[35] Alexander Schwarz, Moritz Ueffing, Yunpei Deng, Xun Gu, Hanieh Fattahi, Thomas Metzger, Marcus Ossiander, Ferenc Krausz, and Reinhard Kienberger. Active stabilization for optically synchronized optical parametric chirped pulse amplification. *Optics Express*, 20(5):5557, 2012.

[36] P.L. Kelley. Self-Focusing of Optical Beams. *Physical Review Letters*, 15(26):1005–1008, 1965.

[37] N Nakano, H Kuroda, T Kita, and T Harada. Development of a flat-field grazing-incidence XUV spectrometer and its application in picosecond XUV spectroscopy. *Applied optics*, 23(14):2386, jul 1984.

[38] Tenio Popmintchev, Ming-Chang Chen, Dimitar Popmintchev, Paul Arpin, Susannah Brown, Skirmantas Alisauskas, Giedrius Andriukaitis, Tadas Balciunas, Oliver D Mücke, Audrius Pugzlys, Andrius Baltuska, Bonggu Shim, Samuel E Schrauth, Alexander Gaeta, Carlos Hernández-García, Luis Plaja, Andreas Becker, Agnieszka Jaron-Becker, Margaret M Murnane, and Henry C Kapteyn. Bright coherent ultrahigh harmonics in the keV x-ray regime from mid-infrared femtosecond lasers. *Science (New York, N.Y.)*, 336(6086):1287–91, jun 2012.

[39] Achut Giree, Mark Mero, Gunnar Arisholm, Marc J J Vrakking, and Federico J Furch. Numerical study of spatiotemporal distortions in noncollinear optical parametric chirped- pulse amplifiers. *Optics Express*, 25(3104):555–559, 2017.

[40] Selcuk Akturk, Xun Gu, Pamela Bowlan, and Rick Trebino. Spatio-temporal couplings in ultrashort laser pulses. *Journal of Optics*, 12(9), 2010.

[41] a Börzsönyi, Z Heiner, M P Kalashnikov, a P Kovács, and K Osvay. Dispersion measurement of inert gases and gas mixtures at 800 nm. *Applied optics*, 47(27):4856–4863, 2008.

[42] Sabine Keiber, Shawn Sederberg, Alexander Schwarz, Michael Trubetskov, Volodymyr Pervak, Ferenc Krausz, and Nicholas Karpowicz. Electro-optic sampling of near-infrared waveforms. *Nature Photonics*, 10(3):159–162, 2016.

[43] P B Corkum, N H Burnett, and M Y Ivanov. Subfemtosecond pulses. *Optics Letters*, 19(22):1870, nov 1994.

[44] H. Vincenti and F. Quéré. Attosecond lighthouses: How to use spatiotemporally coupled light fields to generate isolated attosecond pulses. *Physical Review Letters*, 108(11):1–5, 2012.

[45] T. J. Hammond, Graham G. Brown, Kyung Taec Kim, D. M. Villeneuve, and P. B. Corkum. Attosecond pulses measured from the attosecond lighthouse. *Nature Photonics*, 10(3):171–175, 2016.

[46] Gwyn Williams Albert Thompson, David Attwood, Eric Gullikson, Malcolm Howells, Kwang-Je Kim, Janos Kirz, Jeffrey Kortright, Herman Winick, Ingolf Lindau, Yanwei Liu, Piero Pianetta, Arthur Robinson, James Scofield, James Underwood. X-Ray-Data-Booklet, 2009.

[47] Justin Gagnon. *Attosecond Electron Spectroscopy - Theory and its Applications*. PhD thesis, 2010.

[48] M Schultze, M Fiess, N Karpowicz, J Gagnon, M Korbman, M Hofstetter, S Neppl, a L Cavalieri, Y Komninos, Th Mercouris, C a Nicolaides, R Pazourek, S Nagele, J Feist, J Burgdörfer, a M Azzeer, R Ernstorfer, R Kienberger, U Kleineberg, E Goulielmakis, Ferenc Krausz, and V S Yakovlev. Delay in photoemission. *Science (New York, N.Y.)*, 328(5986):1658–62, jun 2010.

[49] Gelsomina De Stasio, B. Gilbert, T. Nelson, R. Hansen, J. Wallace, D. Mercanti, M. Capozi, P. A. Baudat, P. Perfetti, G. Margaritondo, and B. P. Tonner. Feasibility tests of transmission x-ray photoelectron emission microscopy of wet samples. *Review of Scientific Instruments*, 71(1):11–14, 2000.

Acknowledgments

- First I want to thank Ferenc Krausz for giving me the opportunity to work in his group and to use the extensive infrastructure he was able to build around the group. There are not many places where the things we do are possible.

- Nick Karpowicz, thank you for the awesome support, the countless brilliant ideas, and all the explanations of things I didn't understand. I couldn't have wished for a better direct adviser.

- A big thank you to Matthew Weidman for the patience working with me in the lab and for tolerating my occasional stubbornness, I hope it wasn't too bad. Having a constant partner in the lab made things much easier and improved my motivation during difficult times tremendously. Just talking about what we are doing helped to find new ideas or avoid too stupid mistakes. Additionally, also thank you for the fun we had despite all the work.

- Thank you Hanieh Fattahi for that neccessary bit of crazy around and for all the discussions, fun, and not least the parties.

- Thanks to all the former and newer members of the group around Nick for all the support and for making it a pleasant environment to work in. Sabine Keiber, Olga Razskazovskaya, Shawn Sederberg, Alex Schwarz, Enrico Ridente, Dimitry Zimin, Mikhail Mamaikin.

- The "Atto guys (and girl)" for a nice office and the continued supportive working environment. Marcus Ossiander, Florian Siegrist, Julia Gessner, Keyhan Golyari, Martin Schultze

- Special thanks to Martin Triphahn for his fast and competent help whenever needed, and because I promised. You leaving really was a loss.

- Thanks to the workshop around Michael Rogg. We couldn't build most of what we do without them. Also thanks for all the ideas how to implement things we were imagining and all the quick repairs whenever we screwed up again.

- There are many more who helped with ideas or borrowed equipment. I'm also sure I forgot some. Thanks to all of you.

- Karl Dressler und Elisabeth Simon
- Vielen Dank an meine Eltern. Danke für all die Unterstützung, ohne die ich nicht so weit gekommen wäre und ohne die ich diese Arbeit nicht hätte vollenden können.
- Zu guter Letzt, Lena. Einfach nur danke, dass du da bist.